



## RESEARCH ARTICLE

10.1029/2018JA025245

## Special Section:

Magnetospheric Multiscale (MMS) mission results throughout the first primary mission phase

## Key Points:

- MMS mapped the EDR and near-EDR several times during a sequence of new dayside encounters
- Turbulence in Ohm's law terms is greatest on the magnetospheric-side EDR, near the plane containing the X line and boundary normal vector
- Thirty-two EDR or near-EDR encounters show crescent-like enhancements in electron velocity space perpendicular to the local magnetic field

## Supporting Information:

- Supporting Information S1
- Movie S1
- Movie S2
- Movie S3
- Movie S4
- Movie S5

## Correspondence to:

J. M. Webster,  
james.m.webster@rice.edu

## Citation:

Webster, J. M., Burch, J. L., Reiff, P. H., Daou, A. G., Genestreti, K. J., Graham, D. B., et al. (2018). Magnetospheric Multiscale dayside reconnection electron diffusion region events. *Journal of Geophysical Research: Space Physics*, 123, 4858–4878. <https://doi.org/10.1029/2018JA025245>



Received 24 JAN 2018

Accepted 8 MAY 2018

Accepted article online 14 MAY 2018

Published online 20 JUN 2018

## Magnetospheric Multiscale Dayside Reconnection Electron Diffusion Region Events

J. M. Webster<sup>1</sup> , J. L. Burch<sup>2</sup> , P. H. Reiff<sup>1</sup> , A. G. Daou<sup>1,3</sup> , K. J. Genestreti<sup>4</sup> , D. B. Graham<sup>5</sup> , R. B. Torbert<sup>6</sup> , R. E. Ergun<sup>7</sup> , S. Y. Sazykin<sup>1</sup> , A. Marshall<sup>1</sup> , R. C. Allen<sup>8</sup> , L.-J. Chen<sup>9</sup> , S. Wang<sup>9</sup> , T. D. Phan<sup>10</sup> , B. L. Giles<sup>11</sup> , T. E. Moore<sup>11</sup> , S. A. Fuselier<sup>2,12</sup> , G. Cozzani<sup>13</sup> , C. T. Russell<sup>14</sup> , S. Eriksson<sup>7</sup> , A. C. Rager<sup>11</sup> , J. M. Broll<sup>2,12</sup> , K. Goodrich<sup>7</sup> , and F. Wilder<sup>7</sup> 

<sup>1</sup>Department of Physics and Astronomy, Rice University, Houston, TX, USA, <sup>2</sup>Southwest Research Institute, San Antonio, TX, USA, <sup>3</sup>Deceased 18 May 2018, <sup>4</sup>Space Research Institute, Austrian Academy of Sciences, Graz, Austria, <sup>5</sup>Swedish Institute of Space Physics, Uppsala, Sweden, <sup>6</sup>Institute for the Study of Earth, Oceans, and Space, University of New Hampshire, Durham, NH, USA, <sup>7</sup>Laboratory for Atmospheric and Space Physics, University of Colorado Boulder, Boulder, CO, USA, <sup>8</sup>The Johns Hopkins University Applied Physics Laboratory, Laurel, MD, USA, <sup>9</sup>Astronomy Department, University of Maryland, College Park, MD, USA, <sup>10</sup>Space Sciences Laboratory, University of California, Berkeley, CA, USA, <sup>11</sup>NASA Goddard Space Flight Center, Greenbelt, MD, USA, <sup>12</sup>Space Science Department, University of Texas at San Antonio, San Antonio, TX, USA, <sup>13</sup>Laboratory of Plasma Physics, Pierre and Marie Curie University, Paris, France, <sup>14</sup>Department of Earth, Planetary, and Space Sciences, University of California, Los Angeles, CA, USA

**Abstract** We use high-resolution data from dayside passes of the Magnetospheric Multiscale (MMS) mission to create for the first time a comprehensive listing of encounters with the electron diffusion region (EDR), as evidenced by electron agyrotropy, ion jet reversals, and  $\mathbf{j} \cdot \mathbf{E}' > 0$ . We present an overview of these 32 EDR or near-EDR events, which demonstrate a wide variety of observed plasma behavior inside and surrounding the reconnection site. We analyze in detail three of the 21 new EDR encounters, which occurred within a 1-min-long interval on 23 November 2016. The three events, which resulted from a relatively low and oscillating magnetopause velocity, exhibited large electric fields (up to  $\sim 100$  mV/m), crescent-shaped electron velocity phase space densities, large currents ( $\geq 2 \mu\text{A}/\text{m}^2$ ), and Ohmic heating of the plasma ( $\sim 10$  nW/m<sup>3</sup>). We include an Ohm's law analysis, in which we show that the divergence of the electron pressure term usually dominates the nonideal terms and is much more turbulent on the magnetosphere versus the magnetosheath side of the EDR.

**Plain Language Summary** NASA's Magnetospheric Multiscale (MMS) mission was designed to study magnetic reconnection, a process in which oppositely directed magnetic fields embedded within two neighboring plasma populations annihilate, dumping magnetic energy into the plasmas. Previous missions studying reconnection in space were not fully equipped to analyze how the electrons in the plasma behave near the core of a reconnection site. This study provides MMS researchers with many new reconnection events to dissect, and calls special attention to three events that occurred back to back. Each event included is very unique and helps to fill in another piece of the reconnection puzzle. Perhaps the ultimate goal of these studies is to provide insight into methods of shutting down the reconnection process, which is known to impede attempts toward a stable nuclear fusion engine. A blueprint for stable nuclear fusion could solve mankind's energy needs forever.

### 1. Introduction

Magnetospheric Multiscale (MMS) utilizes naturally occurring Sun-Earth interactions as a laboratory to study magnetic reconnection. The pursuit of in situ measurements of electron motion around and inside the electron diffusion region (EDR) drove much of the mission's motivation and design (Burch et al., 2016). From one of the first EDR encounters, Burch et al. (2016) reported agyrotropic, crescent-shaped electron distributions in the plane of phase space density (PSD) normal to the magnetic field vector. Such crescents constitute a direct observational indication of an EDR (Hesse et al., 2014, 2016) and occur primarily in the region between the X line and the electron flow stagnation point ( $S_e$ ) for the case of asymmetric reconnection at the dayside magnetopause. Burch et al. (2016) further reported the evolution of perpendicular crescents into parallel crescents, also observed in the particle-in-cell (PIC) simulations of Shay et al. (2016). So far, perpendicular crescent-shaped electron PSDs and associated EDR physics have been analyzed in 12 MMS encounters

©2018. The Authors.

This is an open access article under the terms of the Creative Commons Attribution-NonCommercial-NoDerivs License, which permits use and distribution in any medium, provided the original work is properly cited, the use is non-commercial and no modifications or adaptations are made.

(Fuselier et al., 2017), including Chen et al. (2016), Khotyaintsev et al. (2016), and others. Shay et al. (2016) also characterized a bipolar signature of the normal electric field component ( $E_N$ ) seen in their results, where  $\mathbf{E}' (= \mathbf{E} + \mathbf{v}_e \times \mathbf{B})$  closely balanced the electron pressure tensor divergence term ( $\nabla \cdot \vec{P}_e$ ) contribution. The simulations showed that large  $|E_N|$  in both terms was coincident with the electron current sheet to within small fractions of one ion inertial length, especially near the  $X$  line. Observationally, exact agreement of enhanced  $E_N$  and  $-j_M$  does not always occur (Norgren et al., 2016; Torbert et al., 2016). The zero guide-field simulation of Shay et al. (2016) did not report significant values of  $E_N$  on the magnetosheath side of their EDR PIC simulations, instead showing that large  $|E_N|$  was mostly confined to the magnetospheric side of the EDR and separatrix. Other PIC simulations (Hesse et al., 2014, 2016) have predicted a dominance of  $\nabla \cdot \vec{P}_e$  in Ohmic energy conversion near  $S_e$ , but at the  $X$  line, the electron inertial term was expected to dominate, regardless of guide-field strength. Torbert et al. (2016) confirmed large  $\nabla \cdot \vec{P}_e$  values ( $\sim -5$  mV/m) at  $S_e$  for the low guide-field of Burch et al. (2016), and Genestreti et al. (2018) showed that  $\nabla \cdot \vec{P}_e$  also governed Ohmic energy conversion at the  $X$  line for a strong guide-field event. Turbulence seen in 3-D reconnection simulations (Price et al., 2016, 2017) at relatively small scales developed primarily near the  $M$ - $N$  plane of symmetry ( $M$ - $N$  plane passing through the center of the EDR).

For this paper, we scanned the Phase 1 dayside MMS passes to identify additional EDRs and EDR candidates exhibiting crescent-like electron PSD shapes. After a discussion of observational methods (section 2), we present in section 3 a preview of an additional 21 EDR candidate events, listed here for the first time. Our search yielded a series of direct EDR encounters on 23 November 2016, with at least three new events inside a span of  $\sim 1$  min, for which we provide an introductory analysis in section 4. Section 5 summarizes our results.

## 2. Observations

In order to search the data for candidate events, each 3-D electron PSD shown in this study was created from the total electron flux accrued over one 30-ms interval (Pollock et al., 2016). Every PSD plot (Figures 2–4, along with additional figures in the supporting information) shows the volume confined inside of a  $20^\circ$  half-angle cone (focal point at  $v = 0$ ) cross-sectional area revolved  $360^\circ$  around the axis pointing in/out of the page. Time-aliasing effects create spoke-like “fingers” every  $45^\circ$  and indicate that the distribution is changing on timescales faster than the 30 ms acquisition window. The listed times above all PSDs represent the middle of the acquisition window, that is, 15 ms after each new window begins. All PSDs are shown in the rest frame of the spacecraft, with dotted lines designating the computed electron bulk velocity components projected onto the viewing planes. Color contour scaling of the PSD plots is kept constant throughout this publication. The  $v_{\perp 1}$  direction for all PSD figures is defined by the average (taken over the 30 ms acquisition window) electron bulk velocity component perpendicular to the local magnetic field direction. To quantify the agyrotropy we use the agyrotropy index,  $Q$  (Swisdak, 2016), which is defined as

$$Q = \frac{P_{12}^2 + P_{13}^2 + P_{23}^2}{P_{\perp}^2 + 2P_{\perp}P_{\parallel}}, \quad (1)$$

where the pressure tensor is

$$\mathbb{P} = \begin{pmatrix} P_{\parallel} & P_{12} & P_{13} \\ P_{12} & P_{\perp} & P_{23} \\ P_{13} & P_{23} & P_{\perp} \end{pmatrix}. \quad (2)$$

The scaling of  $\sqrt{Q}$  ranges from 0 (no agyrotropy) to 1, and models predict comparatively large values near the EDR.  $\sqrt{Q}_e$  and  $\sqrt{Q}_i$  denote electron and ion agyrotropy, respectively. We use the 128 Hz resolution fluxgate magnetometers (Russell et al., 2016) and  $\sim 8$  kHz resolution search coil magnetometers (Le Contel et al., 2014), and both AC and DC electric field measurements (Ergun et al., 2016; Lindqvist et al., 2016; Torbert et al., 2016) for our analyses. We use “level 2”  $E$ -field data, which have been processed for cross calibration. For the Ohm’s law computations, we use the newly available high-resolution moments data (Rager et al., 2018), with 7.5 ms resolution for electron moments, and 37.5 ms resolution for ion moments. The generalized Ohm’s law equation (Gurnett & Bhattacharjee, 2005) employed here is

$$\vec{E}' = \eta \vec{J} - \frac{1}{en} \nabla \cdot \vec{P}_e + \frac{m_e}{en} \left( \frac{1}{e} \frac{\partial \vec{J}}{\partial t} + \nabla \cdot n (\vec{v}_i \vec{v}_i - \vec{v}_e \vec{v}_e) \right), \quad (3)$$

where  $m_e$  is the electron mass,  $e$  is the fundamental unit of charge,  $n$  is the plasma number density,  $v_e$  is the bulk electron velocity,  $v_i$  is the bulk ion velocity,  $\vec{J}$  is the current density, and  $\eta$  is the anomalous resistivity.  $\vec{E}'$  is the electric field in the electron convective frame. To compute  $\vec{E}'$ , electric field ( $E$  field) measurements are smoothed to the standard resolution (30 ms) electron moments cadence, and no boxcar averaging scheme is applied. We use the conservative form of the Ohm's law equation, such that nonzero values for terms on the right-hand side represent a departure from ideal magnetohydrodynamics. We assume a linear fit to the divergence and gradient computations across the volume of the MMS tetrahedron formation, which is not unreasonable given the 6 km spacing of the spacecraft. The ion inertial contribution (term proportional to  $\nabla \cdot \vec{v}_i \vec{v}_i$ ) was nearly 2 orders of magnitude below that of the electron inertial term for the time period analyzed here, and thus, we do not include it further. The partial time derivative of the current density term is also usually negligible in this formulation. Subtracting the computed right-hand side terms from  $\vec{E}'$  yields the residual  $E$  field ( $\vec{E}_{\text{res}}$ ) and provides a measure of  $\eta \vec{J}$ , but the result also contains errors associated with making the approximations we have listed. Wave-particle interactions are also not included in our Ohm's law formulation, especially for interactions occurring on timescales much shorter than the plasma moment data resolution. A more thorough discussion of Ohm's law analysis errors can be found in Torbert et al. (2016) and Genestreti et al. (2018). Additionally, the interpolation used to produce the high-resolution data can introduce small, artificial oscillations, which are most prominent in the electron pressure tensor divergence when  $n_e$  is small ( $n_e \lesssim 5 \text{ cm}^{-3}$ ); thus, we confine our discussion to qualitative trends and sustained behavior for our Ohm's law analyses during periods of  $n_e \geq 5$ . For comparison, we also compute the Hall  $E$ -field contribution ( $\vec{E}_{\text{Hall}} = \mathbf{j} \times \mathbf{B}$ ), although it does not appear explicitly in equation (3). Taking the scalar product of both sides of the Ohm's law equation allows for a corresponding Ohmic energy exchange analysis. We note that Ohmic energy exchange associated with the Hall term,  $\mathbf{j} \cdot (\mathbf{j} \times \mathbf{B})$ , should always be zero, but we include it in our analysis to show component cancellations.

### 3. Overview of 32 EDR Events From Phase 1

We examine MMS burst data from Phase 1 for occurrences of hot electrons, low  $|\mathbf{B}|$ , DC or fluctuating  $E$  field (waves), ion jet reversals, and large  $+j_y$  (current density in the positive geocentric solar magnetospheric [GSM]  $y$  direction). Candidates usually demonstrated a  $B_z$  component reversal during or immediately surrounding each interval. We acknowledge that imposing the constraint of a small magnetic field ( $B$  field) strength may bias the selections toward small guide-field reconnection (small  $B_M$ ), and checking for this bias will require further effort to obtain appropriate boundary-normal coordinates for each new event. After narrowing down the resulting field of candidates with our criteria, we developed animated data products to search through several tens of thousands of 30 ms duration electron PSDs for agyrotropic, two-fluid, crescent-like shapes. Very rarely did clear signatures of two distinct electron plasma populations appear in the distributions. Fewer than 1 selection in 15 exhibited crescents in electron PSDs within the plane perpendicular to the magnetic field. The physical locations of the new dayside EDR candidates are plotted in Figure 1 using GSM coordinates, along with previously published dayside EDR events (Fuselier et al., 2017). In general, a positive  $y$  component of the interplanetary magnetic field (IMF) produced reconnection events on the dawnward side of the magnetopause, and a negative  $Y$ -component IMF led to duskward reconnection sites. The influence of IMF orientation on reconnection event locations is given closer consideration in the "Maximum Magnetic Shear" model of Trattner et al. (2017). Figure 1 also shows a snapshot from a global magnetohydrodynamics simulation using the 23 November 2016 solar wind conditions, conducted with the BATS-R-US model (Tóth et al., 2005). The plotted magnetic field lines (with the red line closed and the blue in the magnetosheath) are on the verge of reconnection. We infer from the model that magnetic field lines approaching the EDR from both the magnetosheath and magnetosphere sides were distorted into the GSM  $+y$  direction just before reconnecting. We also note that the model predicted the magnetic separator to lie very close to the location of MMS, consistent with our observations of several pronounced and prolonged EDR encounters.

We now present one 3-D electron PSD from each dayside EDR or near-EDR encounter revealed by our analysis, together with 11 of the 12 events from Fuselier et al. (2017). The total number of candidate events is now 34. In this report, we exclude two: the event of Genestreti et al. (2018) was not yet published when our meta-

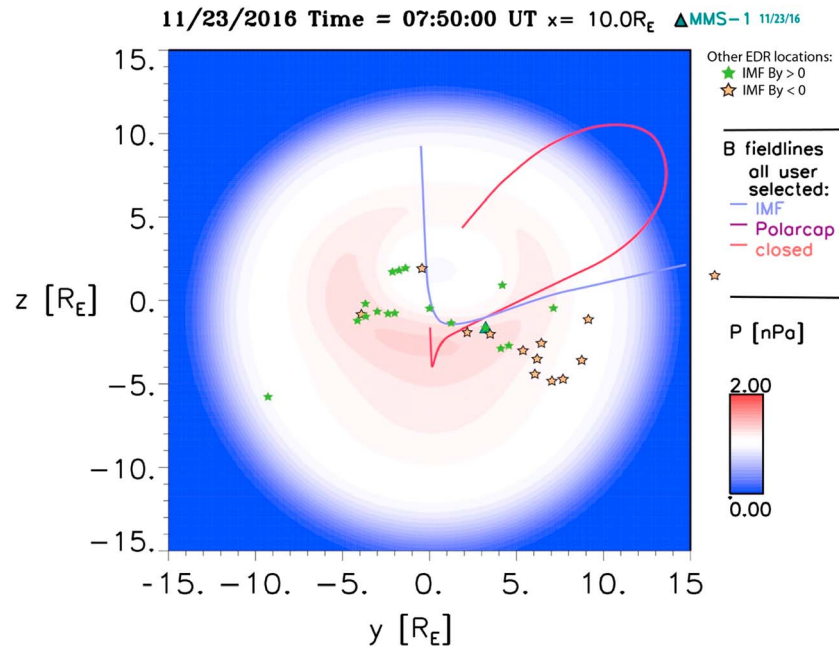


**Figure 1.** GSM Y and Z locations of 32 EDR events or candidate events. The green stars represent positive IMF Y components, and the gold stars represent negative IMF Y components during each event. Magnetic field and dynamic pressure data are taken from a model run of the BATS-R-US global MHD model (CCMC run “James\_Webster\_032117\_1”) with the November 23<sup>rd</sup>, 2016 EDR event solar wind conditions. The viewing plane is  $X = 10 R_E$ , looking toward Earth. Magnetic field line behavior is discussed in section 4.1.

study was conducted, and the Kelvin-Helmholtz event of Eriksson et al. (2016) lacked appreciable crescents in the electron PSD. Because some EDR events have likely been overlooked, we do not claim that the list is exhaustive. Figures 2–4 shows the PSD from the time of the most intense crescent for each event, as three views stacked vertically, with the last in each set repeated in larger scale to see the labels. The top plot for each event is the PSD cut in the plane perpendicular to the magnetic field, with  $\mathbf{v}_{\perp 1}$  along the net electron flow and  $\mathbf{v}_{\perp 2}$  perpendicular to that. It is this top row that demonstrates the agyrotropic crescents, and all crescents are observed on the right-hand side of each of those plots, thus in the direction of maximum perpendicular electron flow  $\mathbf{v}_{\perp 1}$ . The lower two cuts for each event are the  $\mathbf{v}_{\parallel}\mathbf{v}_{\perp 1}$  plane (center) and  $\mathbf{v}_{\parallel}\mathbf{v}_{\perp 2}$  plane (lower). Figure 2 shows events 1–6 in the upper panel and 7–11 in the lower panel. Similarly, Figure 3 shows events 12–22 and Figure 4 shows events 23–32. Examining the middle cut of each (the  $\mathbf{v}_{\parallel}\mathbf{v}_{\perp 1}$  plane), we see that the crescents (which are strong flows in  $\mathbf{v}_{\perp 1}$ ) typically occur only at low values of  $\mathbf{v}_{\parallel}$ . Two good examples of this are events B26 and B27, where the crescent fluxes appear as bumps in this cut at low  $\mathbf{v}_{\parallel}$  above and/or below the main distribution. Thus, the crescents are really partial toroids and not hemispherical shells. Although only one example per EDR candidate event is provided here, most events contain many other 30 ms windows with crescent-like distributions for one or more spacecraft.

We also conduct a preliminary dayside EDR statistical meta-study. We compute and analyze widely studied properties of EDRs for the 32 events. Tables 1 and 2 detail the results. Events are now sorted by row, chronologically, with different computations composing the table’s columns, and the caption offers a brief description of all computations. We use a 4-s computation window, beginning 2 s prior to an event’s “central time,” and lasting 2 s afterward. This central time is generally chosen to lie at the electron PSD time shown in Figures 2–4, rounded to the nearest second. Some exceptions are made in the case of familiarity with a previously published event’s more exact center, which we acknowledge may slightly bias the computations. Each computation is performed first at the individual spacecraft level over the event window, and then the four results are averaged together. As an example, “Avg.  $\sqrt{Q_e}$ ” refers to a calculation in which each individual spacecraft’s electron agyrotropy observations are first averaged over the 4-s window, and then averaged again across the four spacecraft. For the maximum and minimum computations, one max/min value is first found for each spacecraft during the interval (generally not simultaneous), and then averaged across

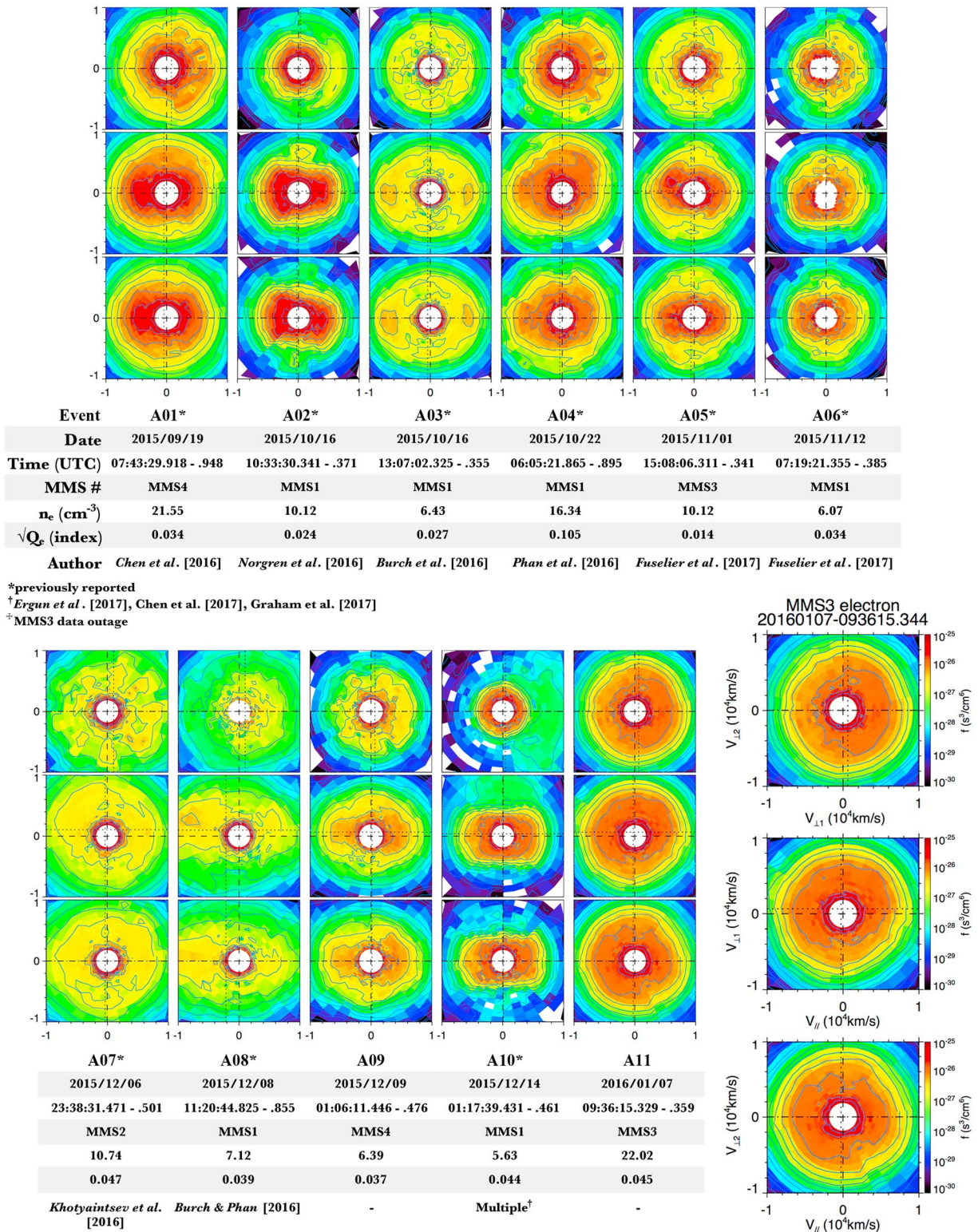


**Figure 2.** Three views of one spacecraft's 3-D electron velocity space distribution for each of 32 events, sorted chronologically, first by column, then by row. Below each column, we assign an event name and list the interval of time over which each distribution function was accumulated. Names beginning with "A" designate Phase 1a events and "B" designates Phase 1b events. We include the spacecraft number, along with the observed density and agyrotropy calculation for the same 30 ms interval. Also shown are the definitions of the axes used in each event's three cross-sectional views, at the bottom right of the figure. The average direction of the local magnetic field during each sample defines the  $+\mathbf{v}_{\parallel}$  direction. The positive  $\mathbf{v}_{\perp 1}$  direction is defined as  $(\mathbf{v}_{\parallel} \times \mathbf{v}_e) \times \mathbf{v}_{\parallel}$ , where  $\mathbf{v}_e$  is the bulk electron velocity's unit vector, here. The  $\mathbf{v}_{\perp 2}$  direction completes a right-handed coordinate system, such that  $\mathbf{v}_{\perp 1} \times \mathbf{v}_{\perp 2} = \mathbf{v}_{\parallel}$ . See section 3 for additional remarks.

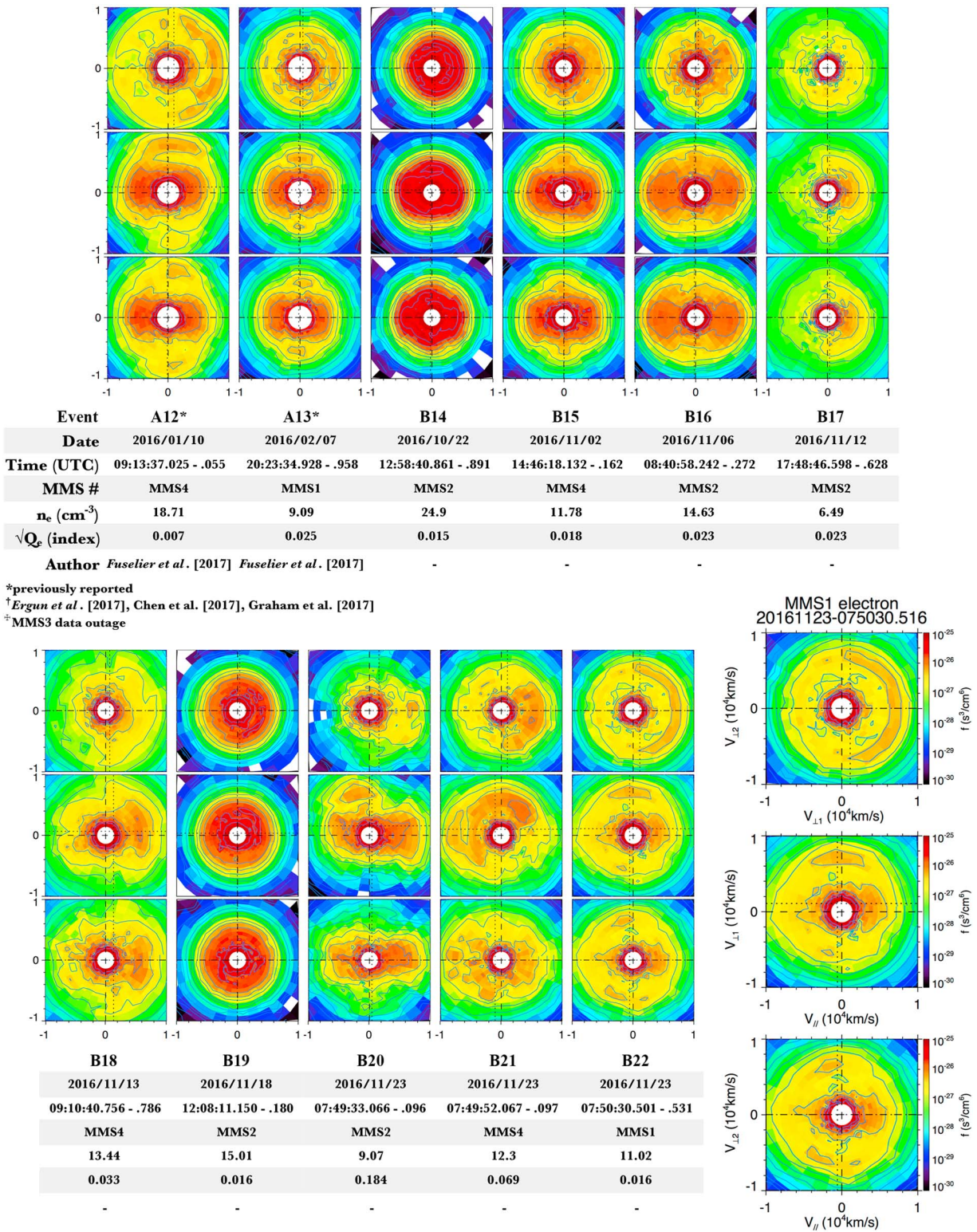
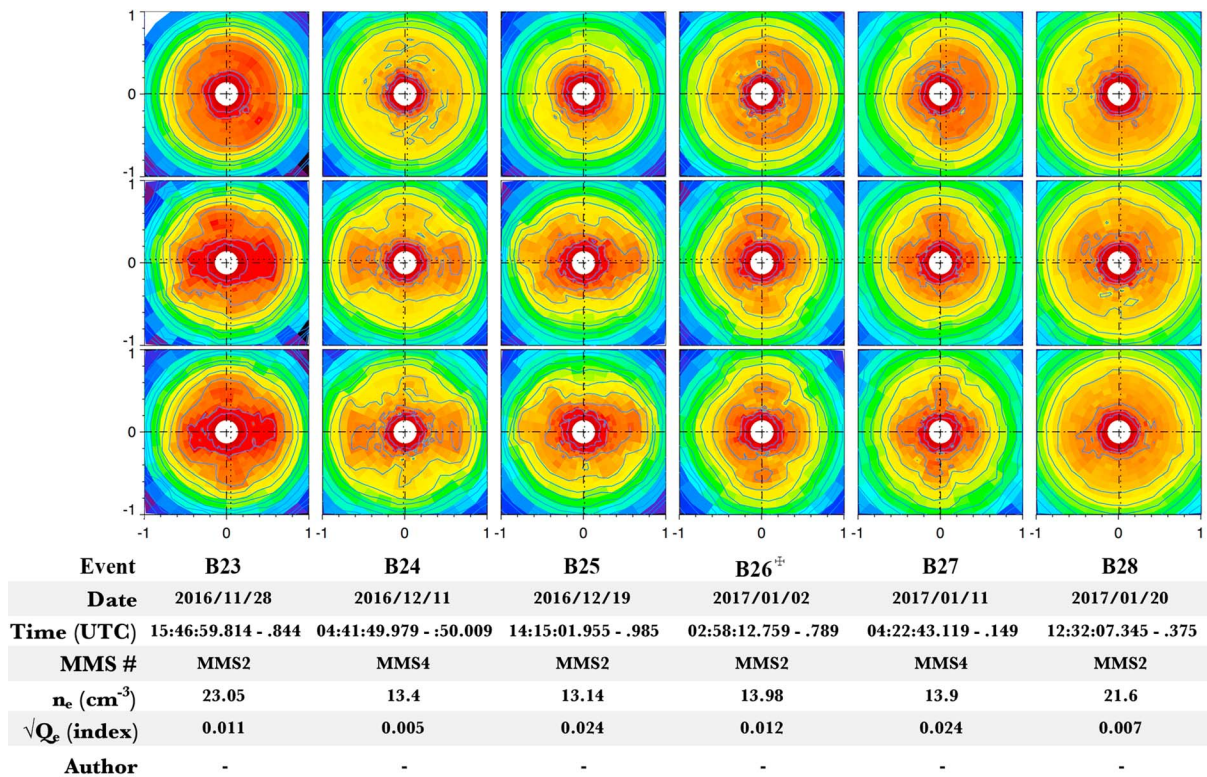


Figure 3. A continuation of Figure 2. See section 3 for additional remarks.

spacecraft. We suggest that the time-averages  $(\langle |j|, \sqrt{Q_e}, \mathbf{j} \cdot \mathbf{E}' \rangle)$  for an event roughly serve as a measure of the accrued amount of time spent by the constellation barycenter/centroid inside the EDR or on the nearby separatrix, scaled by the (local) reconnection rate. The sole exception in completeness of the data set is an



\*previously reported

<sup>†</sup>Ergun *et al.* [2017], Chen *et al.* [2017], Graham *et al.* [2017]

<sup>‡</sup>MMS3 data outage

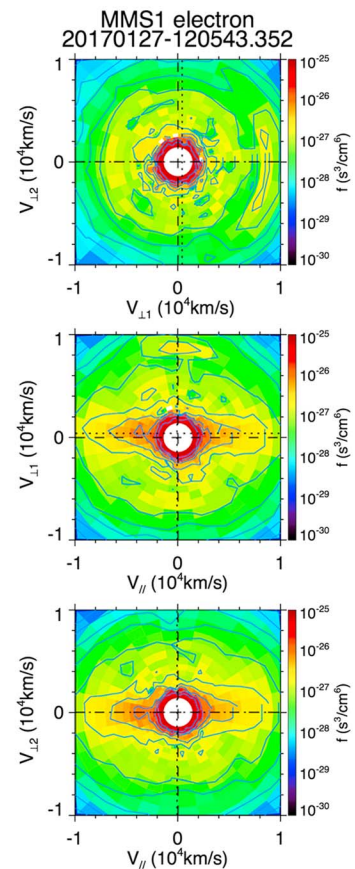
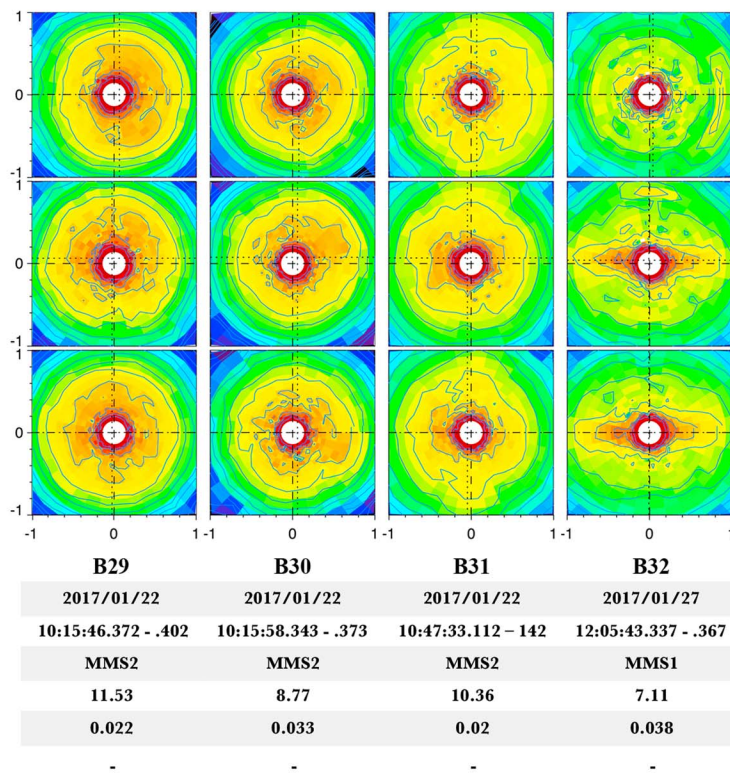


Figure 4. A continuation of Figures 2 and 3. See section 3 for additional remarks.

**Table 1**  
The 32 Selected EDR or Near-EDR Encounters, Sorted in Chronological Order, by Row

Event	Date and time (UTC)	X <sub>GSM</sub> (rE)	Y <sub>GSM</sub> (rE)	Z <sub>GSM</sub> (rE)	Separation (km)	Max ρ <sub>e</sub> (km)	Max ρ <sub>i</sub> (km)	Avg. n <sub>e</sub> (cm <sup>-3</sup> )	Avg  j  (μA * m <sup>-2</sup> ) <sup>a</sup>	Max  j  (μA * m <sup>-2</sup> )	Max j <sub>y</sub> (μA * m <sup>-2</sup> )	Min  B  (nT)
A01 <sup>a</sup>	19/9/2015 07:43:30	6.346	5.399	-2.982	71.57	6.83	1374.9	22.93	0.79	2.73	1.84	10.14
A02 <sup>a</sup>	16/10/2015 10:33:30	9.231	6.092	-4.403	13.87	8.72	1703.8	13.55	0.56	1.20	0.90	2.42
A03 <sup>a</sup>	16/10/2015 13:07:02	8.310	7.078	-4.800	13.78	11.59	2401.1	6.92	0.63	1.85	1.52	2.24
A04 <sup>a</sup>	22/10/2015 06:05:22	9.637	3.481	-1.961	16.93	9.35	509.9	15.17	0.75	2.74	2.46	3.95
A05 <sup>a</sup>	1/11/2015 15:08:06	7.814	6.202	-3.470	14.58	4.25	112.0	9.12	0.71	1.98	1.48	19.49
A06 <sup>a</sup>	12/11/2015 07:19:21	11.507	2.302	-1.776	15.82	8.67	570.8	5.84	0.24	1.06	0.75	3.75
A07 <sup>a</sup>	6/12/2015 23:38:31	8.516	-3.916	-0.810	19.23	5.74	108.3	9.16	0.69	2.82	1.61	19.76
A08 <sup>a</sup>	8/12/2015 11:20:44	10.233	1.288	-1.364	15.30	4.83	174.6	5.12	0.44	2.43	2.15	14.76
A09	9/12/2015 01:06:11	9.922	-3.671	-0.928	17.34	6.10	619.2	8.03	0.37	1.11	0.84	9.85
A10 <sup>a</sup>	14/12/2015 01:17:40	10.131	-4.163	-1.191	16.97	9.46	846.1	5.09	0.49	1.73	1.68	4.49
A11	7/1/2016 09:36:15	8.888	-1.968	-0.733	41.75	7.24	348.7	21.41	0.64	2.18	1.93	8.03
A12 <sup>a</sup>	10/1/2016 09:13:37	8.808	-2.395	-0.775	40.84	6.67	386.4	14.74	0.83	3.75	3.13	9.94
A13 <sup>a</sup>	7/2/2016 20:23:35	3.874	-9.325	-5.720	15.99	10.72	2327.4	8.49	0.18	0.52	0.19	3.06
B14	22/10/2016 12:58:41	6.406	7.700	-4.706	8.87	6.21	331.3	25.49	0.85	2.81	2.17	3.81
B15	2/11/2016 14:46:18	7.241	8.812	-3.543	8.18	6.16	159.7	9.83	0.28	0.90	0.60	8.67
B16	6/11/2016 08:40:58	7.943	4.113	-2.826	11.76	3.00	133.1	13.70	0.96	2.40	1.82	28.89
B17	12/11/2016 17:48:47	6.624	9.165	-1.104	7.35	10.98	432.7	5.04	0.34	0.96	0.70	6.10
B18	13/11/2016 09:10:41	8.958	4.563	-2.625	11.38	5.61	341.7	9.40	0.48	2.92	1.98	18.57
B19	18/11/2016 12:08:11	9.596	6.460	-2.509	4.88	8.40	474.8	15.45	0.54	1.47	1.38	3.21
B20	23/11/2016 07:49:33	9.613	3.232	-1.604	6.43	8.16	413.9	11.61	0.73	2.23	1.56	5.93
B21	23/11/2016 07:49:52	9.613	3.232	-1.604	6.43	4.25	106.9	8.78	1.36	2.96	2.77	22.24
B22	23/11/2016 07:50:30	9.620	3.245	-1.608	6.42	4.66	110.0	9.05	1.04	2.59	2.30	19.90
B23	28/11/2016 15:47:00	8.884	7.184	-0.440	6.32	4.80	150.6	16.94	0.33	1.80	0.46	12.99
B24	11/12/2016 04:41:50	9.489	-0.056	-0.448	6.89	7.79	400.0	13.10	0.35	0.90	0.74	8.03
B25	19/12/2016 14:15:02	10.204	4.170	0.934	8.42	7.90	669.9	11.12	0.42	1.00	0.84	5.52
B26 <sup>b</sup>	2/1/2017 02:58:13	9.647	-3.007	-0.649	9.96	8.50	761.0	12.71	0.37	0.89	0.78	4.30
B27	11/1/2017 04:22:43	10.809	-3.713	-0.154	8.17	9.10	488.5	13.16	0.33	1.66	0.95	5.14
B28	20/1/2017 12:32:07	9.634	-0.461	1.967	6.47	9.27	485.1	16.51	0.72	1.96	1.25	6.01
B29	22/1/2017 10:15:46	10.744	-2.138	1.766	5.75	13.70	1006.4	10.78	0.45	1.82	1.63	2.35
B30		10.750	-2.148	1.764	5.74	9.99	475.9	9.79	0.47	1.29	1.17	4.53



**Table 1** (continued)

Event	Date and time (UTC)	$X_{\text{GSM}}$ (rE)	$Y_{\text{GSM}}$ (rE)	$Z_{\text{GSM}}$ (rE)	Separation (km)	Max $\rho_e$ (km)	Max $\rho_i$ (km)	Avg. $n_e$ ( $\text{cm}^{-3}$ )	Avg $ j $ ( $\mu\text{A} * \text{m}^{-2}$ ) <sup>a</sup>	Max $ j $ ( $\mu\text{A} * \text{m}^{-2}$ )	Max $j_y$ ( $\mu\text{A} * \text{m}^{-2}$ )	Min $ B $ (nT)
	22/1/2017 10:15:58											
B31	22/1/2017 10:47:33	10.519	-1.790	1.837	5.86	7.48	391.9	9.59	0.44	1.17	0.97	11.43
B32	27/1/2017 12:05:43	9.270	-1.370	1.964	6.05	13.22	1054.9	7.27	0.47	1.49	1.23	2.95

Note. These quantities were first computed at the individual spacecraft level, over a 4-s interval spanning  $\pm 2$  s around each event's "central time" (see section 3). Each spacecraft's result was then averaged to produce the numbers provided here. Column 1 (C1) lists the event name assignments, and Column 2 (C2) designates each event's central time. C3, C4, and C5 are the X, Y, and Z positions of the MMS centroid, in GSM coordinates, and C6 is the spacecraft separation. The maximum electron gyroradius is listed in C7, and C8 gives the max for the ion gyroradius. C9 is the average electron number density. C10 and C11 are the average and maximum current densities, respectively; C12 is the maximum value of the GSM Y component of the current; and C13 is the smallest B-field magnitude.  
<sup>a</sup>Previously reported. <sup>b</sup>MMS3 data outage.

exclusion of MMS3 data during encounter B26 due to a timing accuracy error, and thus, only the other three spacecraft results were averaged together. We attempt to prevent events with spacecraft trajectories predominantly through the magnetosphere from artificially inflating  $\sqrt{Q_e}$  statistics by excluding values of  $\sqrt{Q_e}$  in the table's computations for data points when  $n_e < 5 \text{ cm}^{-3}$ . Off-diagonal values in the pressure tensor are easier to increase (relative to the diagonal's values) for a plasma of lower density and dominant  $T_{e \parallel}$ , a condition commonly found in the outer magnetosphere. Argall et al. (2018) also reported artificial enhancements of  $\sqrt{Q_e}$  for periods of small electron flux.

The plots of Figure 5 are examples of simple first-order/linear correlation factors computed from values listed in Tables 1 and 2. All five plots use the average of  $\sqrt{Q_e}$  on the horizontal axis. A generally positive correlation of the average  $\sqrt{Q_e}$  with the five other measurables in Figure 5 is expected, but additional complexities due to turbulence (Ergun et al., 2017), a wide assortment of reconnection conditions (e.g., reconnection rate and guide-field component), and various spacecraft trajectories relative to the EDR prevent a perfect 1-to-1 correlation between any two of our simple indicators. We feature Burch et al.'s (2016) 16 October 2015 EDR event (A03), represented by the green data point in each correlation plot, and the 23 November 2016 events, for easy comparison: B20 (Event "1"; section 4.3.1), B21 (Event "2"; section 4.3.2), and B22 (Event "3"; section 4.3.3), in yellow, magenta, and orange colors, respectively. These four events rank within the top seven highest average agyrotropy measurements. B21 contains especially large  $\mathbf{j} \cdot \mathbf{E}'$  and parallel  $\mathbf{E}$  statistics, suggesting a prolonged fast reconnection rate. An analysis in the supporting information reaffirms this assumption.

#### 4. The 23 November 2016 EDR Events

On 23 November 2016, the MMS spacecraft trajectory intersected the EDR several times. Widely accepted features of EDRs were seen during at least three instances, including thin current sheets (Drake et al., 1994), small  $|B|$ , significant Ohmic energy exchange ( $\mathbf{j} \cdot \mathbf{E}'$ ), large  $\sqrt{Q_e}$ , notable wave activity, and crescent-shaped electron velocity distributions.

##### 4.1. Conditions

We first review the solar wind conditions, location and timing of the event, and the spacecraft constellation configuration, as can be seen in Figure 6. On 23 November 2016, at approximately 07:50 UT, MMS was located near the nominal magnetopause (thin line in beige band in Figure 6a) while traveling outbound, several Earth radii duskward of the subsolar point in the geocentric solar ecliptic X-Y plane. We observe a steady dynamic pressure supplied by the solar wind, and a significant, sustained, southward IMF component ( $B_z \sim -2$  nT), given in GSM coordinates (Figure 6b). The steadiness of the flow pressure and magnetic field acted to confine the EDR within a relatively small volume.

In our analysis of this particular event, we transform the vector data into a boundary-normal coordinate system. Our coordinate transformation was obtained using the "Minimization of Faraday Residue" (MFR) method (Khrabrov & Sonnerup, 1998). The transform, given in base GSM coordinates, is  $L = [0.317, 0.391, 0.864]$ ,  $M = [0.264, -0.911, 0.316]$ ,  $N = [0.917, 0.136, -0.373]$ , and was found by averaging the results of the MFR

**Table 2**  
A Continuation of Table 1

Event	Date and time (UTC)	Max $E_{\parallel}$ ( $\text{mV} \cdot \text{m}^{-1}$ )	Avg. $T_e$ (eV)	Min $T_{e\parallel}/T_{e\perp}$ (ratio)	Max $T_{e\parallel}/T_{e\perp}$ (ratio)	Avg. $\mathbf{j} \cdot \mathbf{E}'$ ( $\text{nW} \cdot \text{m}^{-3}$ )	Max $\mathbf{j} \cdot \mathbf{E}'$ ( $\text{nW} \cdot \text{m}^{-3}$ )	Int. $\mathbf{j} \cdot \mathbf{E}'$ ( $\text{nW} \cdot \text{m}^{-3}$ )	Avg. $\sqrt{Q_e}$ (index)	Max $\sqrt{Q_e}$ (index)
A01 <sup>a</sup>	19/9/2015 07:43:30	16.45	46.4	0.87	2.01	0.057	6.05	12.70	0.017	0.060
A02 <sup>a</sup>	16/10/2015 10:33:30	7.80	36.6	0.84	2.00	0.244	2.42	6.66	0.017	0.052
A03 <sup>a</sup>	16/10/2015 13:07:02	105.94	66.1	0.92	2.22	0.117	22.57	26.24	0.030	0.090
A04 <sup>a</sup>	22/10/2015 06:05:22	48.06	51.8	0.66	1.83	-0.342	7.47	16.93	0.018	0.069
A05 <sup>a</sup>	1/11/2015 15:08:06	29.44	53.2	0.68	2.01	0.217	4.15	8.95	0.023	0.072
A06 <sup>a</sup>	12/11/2015 07:19:21	2.82	45.8	0.90	1.75	0.002	0.97	0	0.018	0.086
A07 <sup>a</sup>	6/12/2015 23:38:31	109.77	111.9	0.58	2.81	0.563	10.13	23.88	0.022	0.066
A08 <sup>a</sup>	8/12/2015 11:20:44	60.68	86.1	0.97	4.43	0.163	8.31	18.01	0.026	0.084
A09	9/12/2015 01:06:11	20.91	64.2	0.95	2.46	-0.422	1.07	0	0.019	0.051
A10 <sup>a</sup>	14/12/2015 01:17:40	63.73	103.1	0.93	2.80	0.577	7.13	15.16	0.031	0.095
A11	7/1/2016 09:36:15	3.30	67.0	1.05	1.81	0.759	6.78	32.95	0.017	0.047
A12 <sup>a</sup>	10/1/2016 09:13:37	51.93	73.1	0.69	2.39	0.924	13.98	55.33	0.022	0.066
A13 <sup>a</sup>	7/2/2016 20:23:35	7.66	56.5	0.79	1.48	0.055	0.38	0	0.016	0.057
B14	22/10/2016 12:58:41	52.27	27.1	0.90	2.80	0.848	11.92	61.31	0.019	0.055
B15	2/11/2016 14:46:18	16.38	46.9	0.89	1.65	-0.089	1.09	0	0.016	0.036
B16	6/11/2016 08:40:58	44.14	58.7	1.54	2.97	0.445	8.12	20.52	0.037	0.075
B17	12/11/2016 17:48:47	38.55	133.5	0.77	1.97	-0.213	5.12	6.24	0.014	0.048
B18	13/11/2016 09:10:41	36.17	88.9	0.81	1.51	0.206	18.28	48.20	0.011	0.050
B19	18/11/2016 12:08:11	5.10	42.7	0.99	2.93	0.043	1.02	0	0.016	0.050
B20	23/11/2016 07:49:33	8.83	67.8	0.71	3.49	0.445	7.35	19.47	0.024	0.121
B21	23/11/2016 07:49:52	133.36	94.5	1.19	3.78	3.130	32.32	124.23	0.031	0.089
B22	23/11/2016 07:50:30	33.59	86.6	0.88	3.55	0.733	8.57	26.44	0.031	0.078
B23	28/11/2016 15:47:00	11.82	45.0	1.04	3.10	0.077	1.63	0.63	0.015	0.036
B24	11/12/2016 04:41:50	2.85	77.7	0.73	1.99	0.342	2.07	2.20	0.010	0.026
B25	19/12/2016 14:15:02	27.59	61.6	0.95	3.06	0.146	2.33	2.33	0.016	0.050
B26 <sup>b</sup>	2/1/2017 02:58:13	8.24	57.2	0.65	1.55	0.375	2.37	21.98	0.012	0.026
B27	11/1/2017 04:22:43	5.07	67.1	0.85	1.33	0.416	8.53	25.98	0.010	0.055
B28	20/1/2017 12:32:07	97.06	90.2	0.97	2.62	1.480	8.31	78.36	0.015	0.051
B29	22/1/2017 10:15:46	19.70	70.4	0.58	2.36	0.414	4.13	20.23	0.018	0.043
B30		10.19	72.7	0.94	2.26	0.214	3.39	5.40	0.017	0.044

**Table 2** (continued)

Event	Date and time (UTC)	Max $E_{\parallel}$ (mV * m <sup>-1</sup> )	Avg. $T_e$ (eV)	Min $T_{e\parallel}/T_{e\perp}$ (ratio)	Max $T_{e\parallel}/T_{e\perp}$ (ratio)	Avg. $\mathbf{j} \cdot \mathbf{E}'$ (nW * m <sup>-3</sup> )	Max $\mathbf{j} \cdot \mathbf{E}'$ (nW * m <sup>-3</sup> )	Int. $\mathbf{j} \cdot \mathbf{E}'$ (nW * m <sup>-3</sup> )	Avg. $\sqrt{Q_e}$ (index)	Max $\sqrt{Q_e}$ (index)
	22/1/2017 10:15:58									
B31	22/1/2017 10:47:33	16.16	92.1	0.82	1.43	0.179	1.98	1.38	0.011	0.036
B32	27/1/2017 12:05:43	12.65	95.1	0.90	1.61	0.447	7.51	62.75	0.015	0.046

Note. Column 1 (C1) relists the event name assignments, and Column 2 (C2), the “central” times. C14 is the maximum  $E$ -field measured parallel to  $\mathbf{B}$ , and C15 is the average electron temperature. C16 and C17 are the minimum and maximum ratios of electron temperature parallel and perpendicular to  $\mathbf{B}$ . C18 is the average  $\mathbf{j} \cdot \mathbf{E}'$ , C19 the max, and C20 is the integrated  $\mathbf{j} \cdot \mathbf{E}'$ , defined as the accrued  $\mathbf{j} \cdot \mathbf{E}'$  over the longest consecutive set of 30-ms intervals exceeding a threshold of 2 nW a m<sup>-3</sup>. Some events do not contain  $\mathbf{j} \cdot \mathbf{E}' > 2$  observed by any spacecraft, translating into “0” values. C21 and C22 are the average and maximum agyrotropy. Agyrotropy measurements for data points of  $n_e < 5 \text{ cm}^{-3}$  were not included in our computations (section 3). We note again that all quantities are the averages across the four spacecraft.

<sup>a</sup>Previously reported. <sup>b</sup>MMS3 data outage.

calculation for the four individual spacecraft, performed over the interval from 07:49:40 UT to 07:50:15 UT. Using this transform, spacecraft relative positions are then rotated into boundary-normal coordinates in Figure 6c, with the location of the centroid of the constellation defining the plot’s origin. For the thin current sheet structures near the EDR, relative spacecraft positions along the  $N$  axis should play an especially important role in the observations. Note that MMS1 and MMS4 differed by less than 1 km in their  $N$  coordinates, while MMS2 sampled conditions  $\sim 5$  km earthward ( $-N$  direction), with MMS3 located in between. The use of this coordinate system throughout our analyses allows for a convenient comparison between the three EDR events.

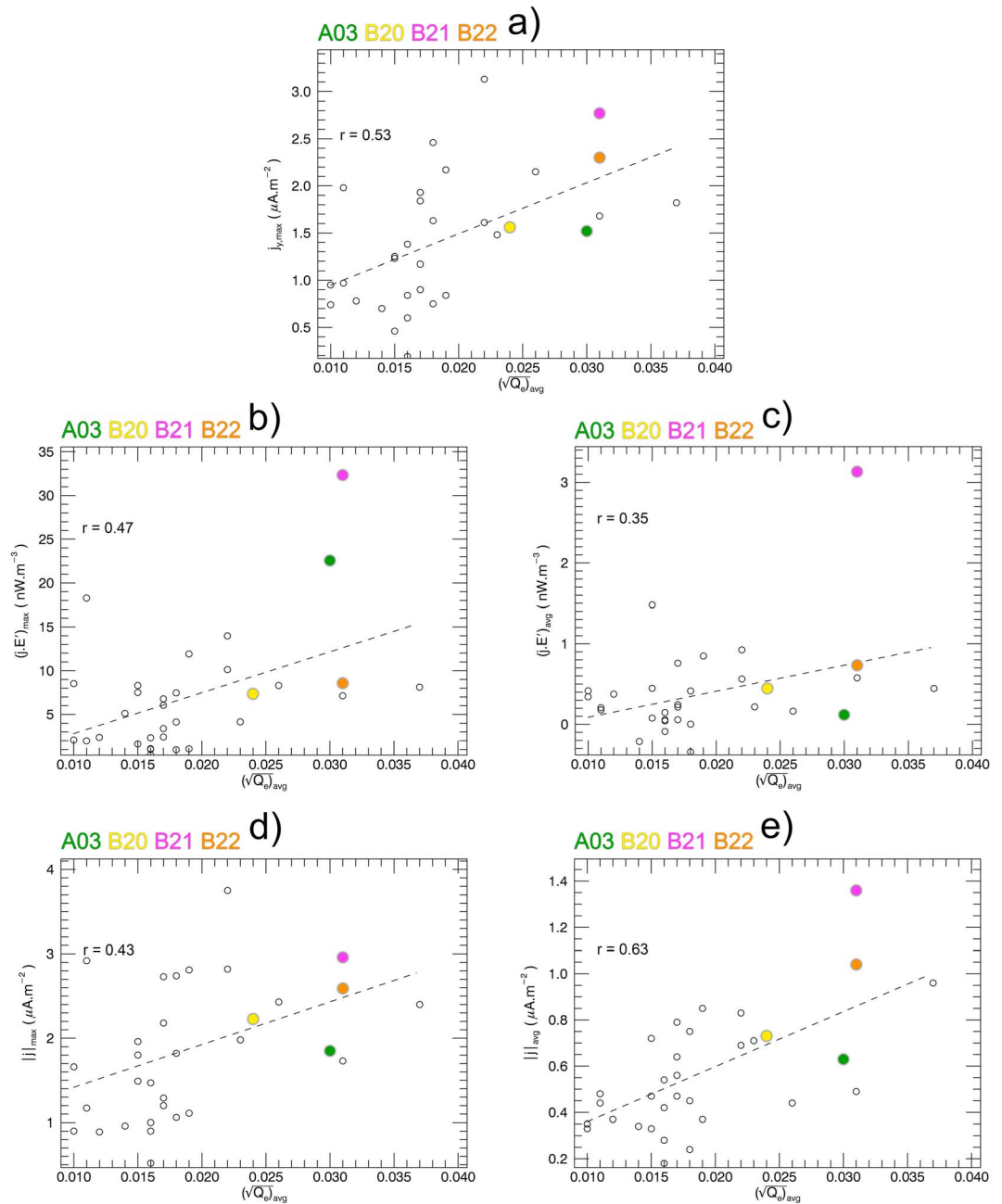
## 4.2. Overview

Figure 7 shows a 1.5-min overview plot of the 23 November EDR events, displaying the data from MMS3, as it represents the location nearest the MMS centroid in the  $N$  direction. We see that the MMS constellation initially resided in the magnetosheath (negative  $B_L$ , large  $n_e$ ), then passed into the magnetosphere near 07:49:35 UT, and eventually returned back to the sheath by  $\sim 07:50:40$  UT. Note that  $n_i$  and  $\sqrt{Q_i}$  are plotted in panel (viii), and  $n_e$  and  $\sqrt{Q_e}$  are plotted in panel (ix). Large measurements of  $-B_M$  (roughly the  $+Y$  GSM direction) occurred throughout the interval, occasionally even comprising the dominant  $B$ -field component, despite the lack of a significant  $Y$  component in the IMF (Figure 6b). Large  $-B_M$  near the reconnection site is consistent with the results of the global model run (Figure 1). Electric and magnetic field waves were strong throughout Figure 7, particularly near the lower hybrid frequency ( $f_{lh}$ ) during events 2 and 3, but also extending above the electron cyclotron frequency ( $f_{ce}$ ) for the  $E$  field. The  $E$ -field waves showed the largest amplitudes and frequencies for durations of time that the spacecraft were inside the magnetosphere and nearest an energetic EDR (see section 4.3.2), at approximately 07:49:52 UT. Rapid-onset ion jet reversals (Petrinec et al., 2016), agyrotropy in both ions and electrons, heated populations, and large  $|\mathbf{j}|$  and  $|\mathbf{j} \cdot \mathbf{E}'|$  all occurred inside of our three designated EDR events. Although many interesting signatures exist throughout the 90 s plot, we will primarily concentrate on observations confined within these three intervals.

## 4.3. EDR Events

### 4.3.1. Event “1”

The first encounter occurred at 07:49:33 UT, when the EDR location moved southward toward the spacecraft, inferred by the ion jet of large  $-v_{iL}$  values beginning to taper toward zero in panel (v) of Figure 7. MMS passed through the in-plane magnetic null point, and then moved into the magnetosheath immediately bordering an active EDR (The supporting information provides an in-depth analysis, and builds on the efforts of previous studies (Argall et al., 2018; Burch et al., 2016b; Cattell et al., 2005; Chen et al., 2017; Drake et al., 2003; Ergun et al., 2017; Graham et al., 2017; Hwang et al., 2013; Kellogg et al., 2010; Khotyaintsev, 2010; Rager et al., 2017; Shay et al., 2016; Tang et al., 2013)). An Ohm’s law analysis of event 1 (Figure 8) shows that  $\nabla \cdot \vec{P}_e$  dominated the nonideal terms of equation (3), with the largest amplitudes in the  $N$  direction. The  $N$  component of  $\mathbf{E}'$  trended with  $E_N$  produced by  $\nabla \cdot \vec{P}_e$  throughout the interval, with both showing large and sustained  $+E_N$  ( $\sim 5$  mV/m) for periods when MMS resided in the electron current layer ( $j_M \leq -0.5 \mu\text{A/m}^2$ ) near the  $X$  line and in the bordering



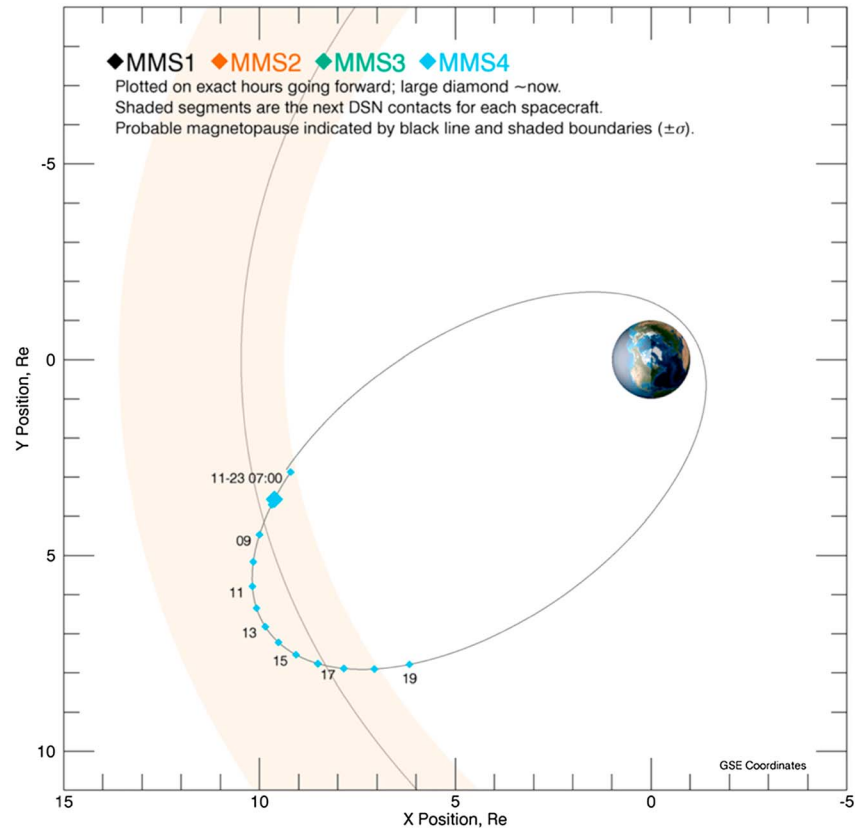
**Figure 5.** Five quantities correlated against the 4 s average of  $\sqrt{Q_e}$ . All values are taken from Tables 1 and 2. (a) Max  $+j_y$  as a function of avg.  $\sqrt{Q_e}$ , (b) Max  $\mathbf{j} \cdot \mathbf{E}'$  versus avg.  $\sqrt{Q_e}$ , (c) The avg. of  $\mathbf{j} \cdot \mathbf{E}'$  versus avg.  $\sqrt{Q_e}$ , (d) Max  $|\mathbf{j}|$  versus avg.  $\sqrt{Q_e}$ , (e) Avg.  $|\mathbf{j}|$  versus avg.  $\sqrt{Q_e}$ . Four data points in each plot are colored, corresponding to event A03 (green), event B20 (yellow), event B21 (magenta), event B22 (orange).

magnetosheath ( $B_L < 0$ ). The events of Torbert et al. (2016) and Norgren et al. (2016) recorded comparable instances. Ohmic energy conversion was well organized inside of the current sheet near the X line (see the supporting information), and energy conversion associated with  $\nabla \cdot \vec{\mathcal{P}}_e$  generally dominated all other energy conversion terms, including  $\mathbf{j} \cdot \mathbf{E}'$ , similar to the X line event of Genestreti et al. (2018).

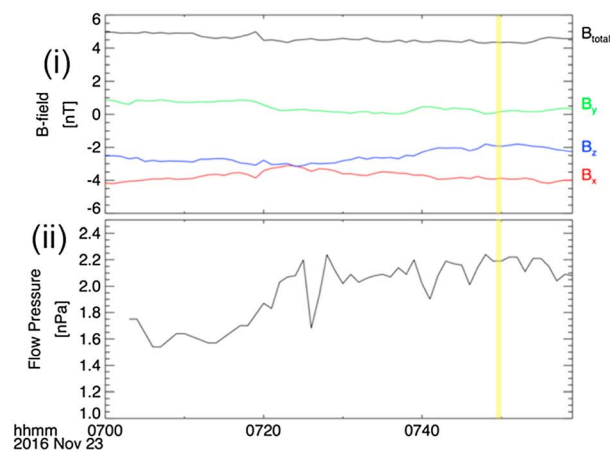
#### 4.3.2. Event “2”

Following event 1, MMS resided in the magnetopause south of the reconnection system for another 20 s ( $-v_{iL}$  values; see Figure 7) on the magnetosphere side ( $+B_L$ ). MMS then made a direct approach to the EDR from the

a) MMS Location for 2016-11-23T07:49:50Z UTC



b) OMNI Data



c) LMN Formation

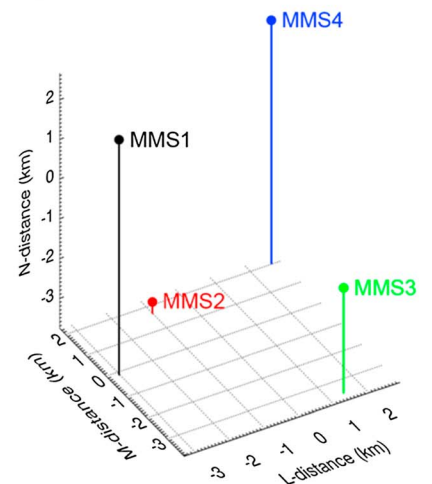


**Figure 6.** The 23 November 2016 event conditions. (a) MMS location relative to Earth and the average magnetopause boundary, shown in GSE, in units of Earth radii. (b) Beginning at 07:00 UTC, a 1 hr plot of the solar wind conditions. Panel (i) plots the IMF magnitude, in black, and the X, Y, and Z (GSM) components in red, green, and blue, respectively. Panel (ii) shows dynamic/ram pressure. The highlighted subinterval designates 07:49 to 07:50, the approximate timing leading up to the 23 November 2016 EDR events. (c) Relative spacecraft positions in LMN coordinates (see section 4.1), in kilometer. The origin is placed at the constellation's centroid. MMS1 is black, MMS2 is red, MMS3 is green, and MMS4 is blue.

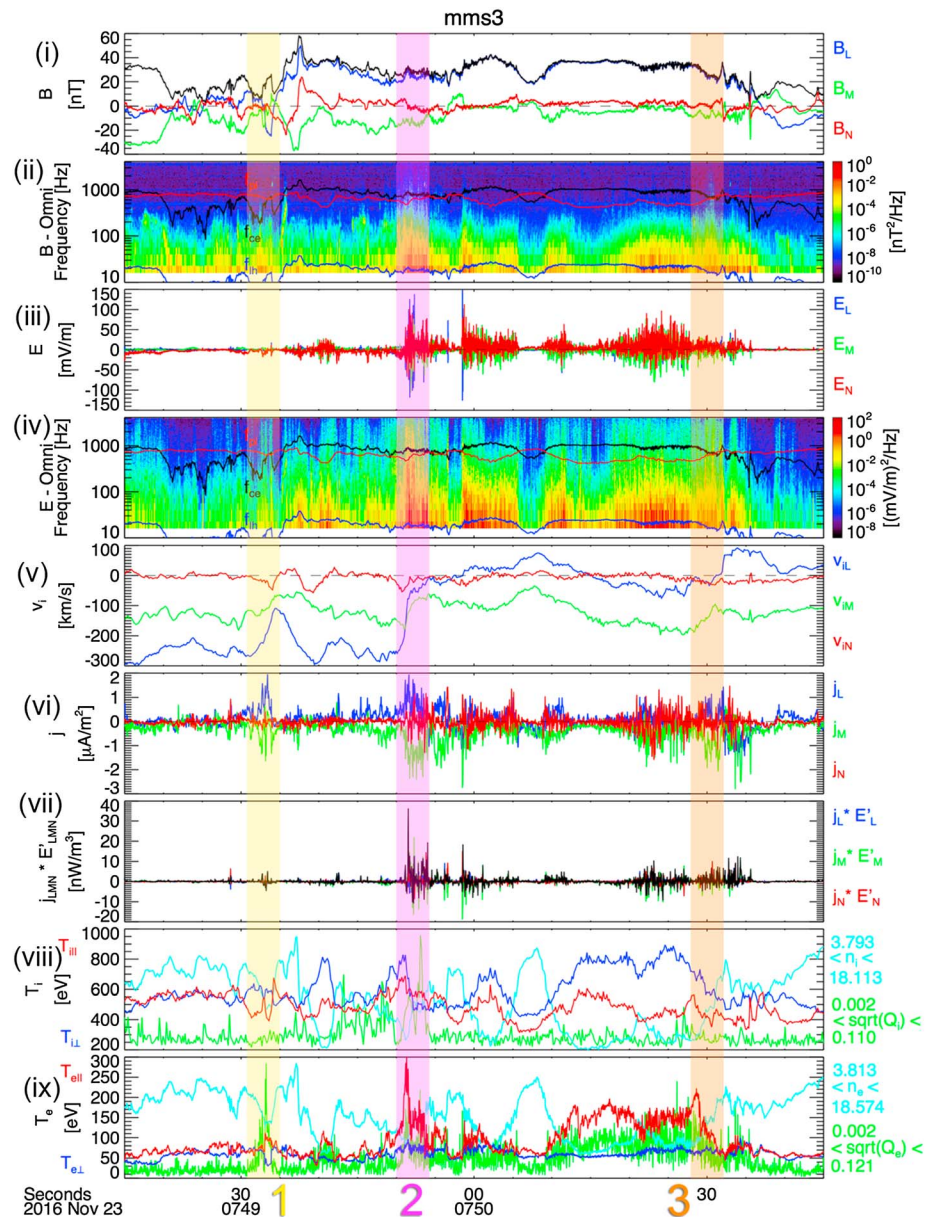


**Figure 7.** MMS3's overview of the EDR observations on 23 November 2016. The vector components are given in  $LMN$  coordinates ( $L = \text{blue}$ ,  $M = \text{green}$ ,  $N = \text{red}$ ), and the black traces indicate a vector's total magnitude. Panel (i) shows the  $B$  field, and panel (ii) shows the  $B$ -field wave spectrogram. Similarly, panel (iii) shows the  $E$  field and panel (iv) shows the  $E$ -field wave spectrogram. The spectrograms also show the computed frequencies of  $f_{lh}$  (lower hybrid, blue),  $f_{ce}$  (electron cyclotron, black), and  $f_{pi}$  (ion plasma, red). Panel (v) plots the ion velocity, (vi) is  $\mathbf{j}$ , (vii) is  $\mathbf{j} \cdot \mathbf{E}$ , and (viii) shows the ion temperature components relative to the local magnetic field, plotted with the ion density ( $n_i$ ) and ion agyrotropy ( $\sqrt{Q_i}$ ) scaled to lie within the panel. The maximum and minimum values of  $n_i$  and  $\sqrt{Q_i}$  within the plotted timespan are listed to the right of the panel, to aid in interpretation. Panel (ix) keeps the same convention used for (viii), applied to the electrons. EDR event timings are indicated by a number and corresponding color (1 = yellow, 2 = magenta, 3 = orange).

magnetospheric side, indicated by a very abrupt cessation of the  $-v_{iL}$  ion jet at  $\sim 07:49:51$  UT. See the supporting information for additional details. We perform an Ohm's law analysis for event 2, shown in Figure 9. Large-amplitude spikes ( $\sim 10$  to  $20$  mV/m) seen in the  $\nabla \cdot \vec{P}_e$  term greatly exceed the other terms (equation (3)). Using the standard 30 ms electron moments resolution (and 150 ms resolution ion moments) with a boxcar averaging scheme reduces the largest peaks to  $\sim 10$  mV/m (not shown), but even those values are still a factor of 2 to 3 times greater than an earlier study employing the same resolution and smoothing scheme (Torbert et al., 2016). The Hall electric field term and the electron inertial term were

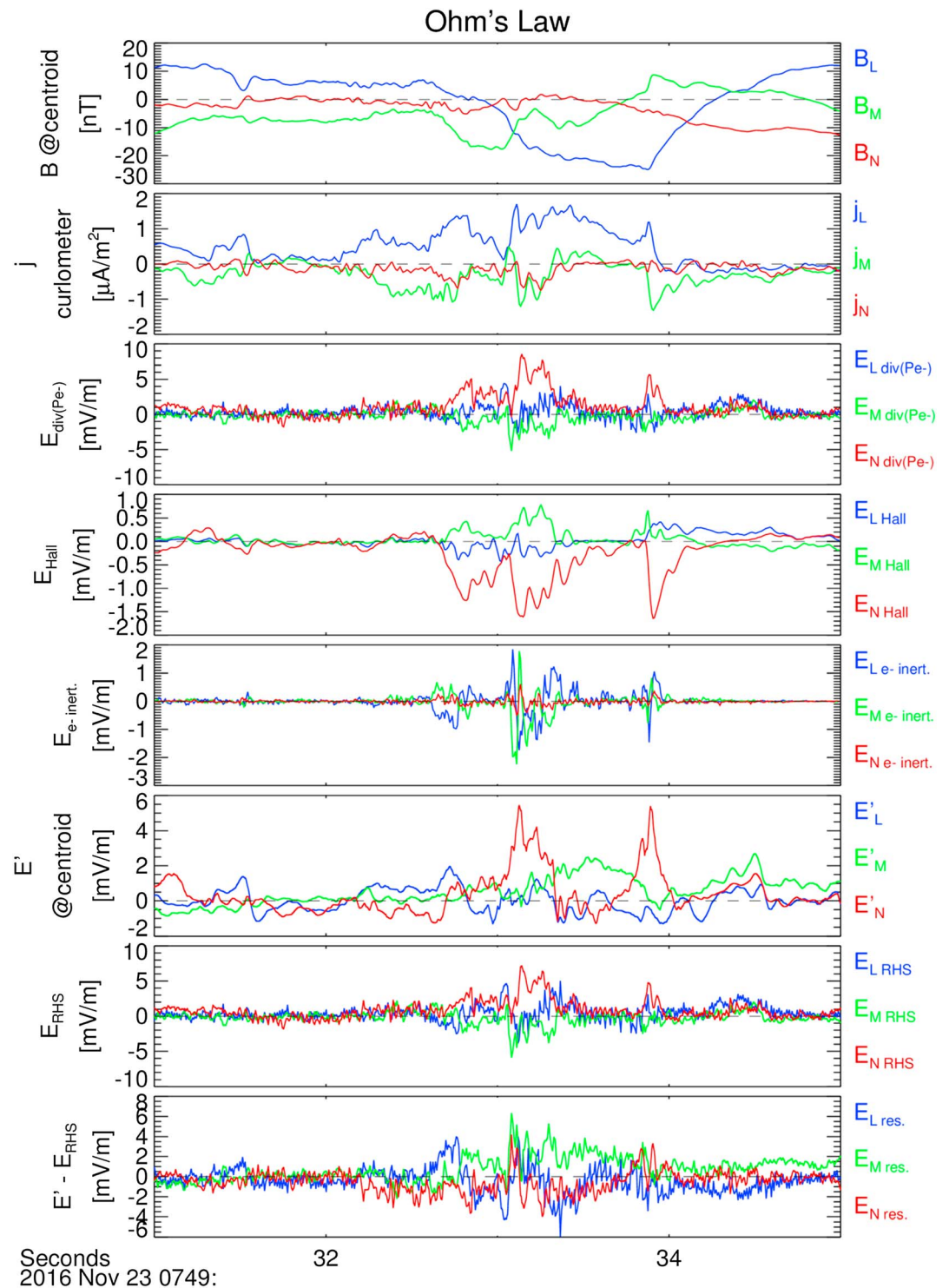


**Figure 8.** Ohm's law analysis during event 1. Panel (i) is the  $B$  field, panel (ii) is the current density yielded via the curlometer technique, panel (iii) is the spatial divergence of the electron pressure tensor term, panel (iv) is the Hall  $E$ -field term, panel (v) is the electron inertial term, panel (vi) is the spacecraft-averaged  $\mathbf{E}'$  at the constellation barycenter, panel (vii) is a summation of (iii) + (iv) + (v), and panel (viii) is the residual  $E$  field, the difference of (vi) minus (vii).

scaled up by a similar amount when compared to two previously published reports (Genestreti et al., 2018; Torbert et al., 2016), but  $\mathbf{E}'$  here was usually of similar magnitude (several mV/m). Although we have commented on some trends, we posit that the 23 November magnetosphere-side Event 2 location is likely

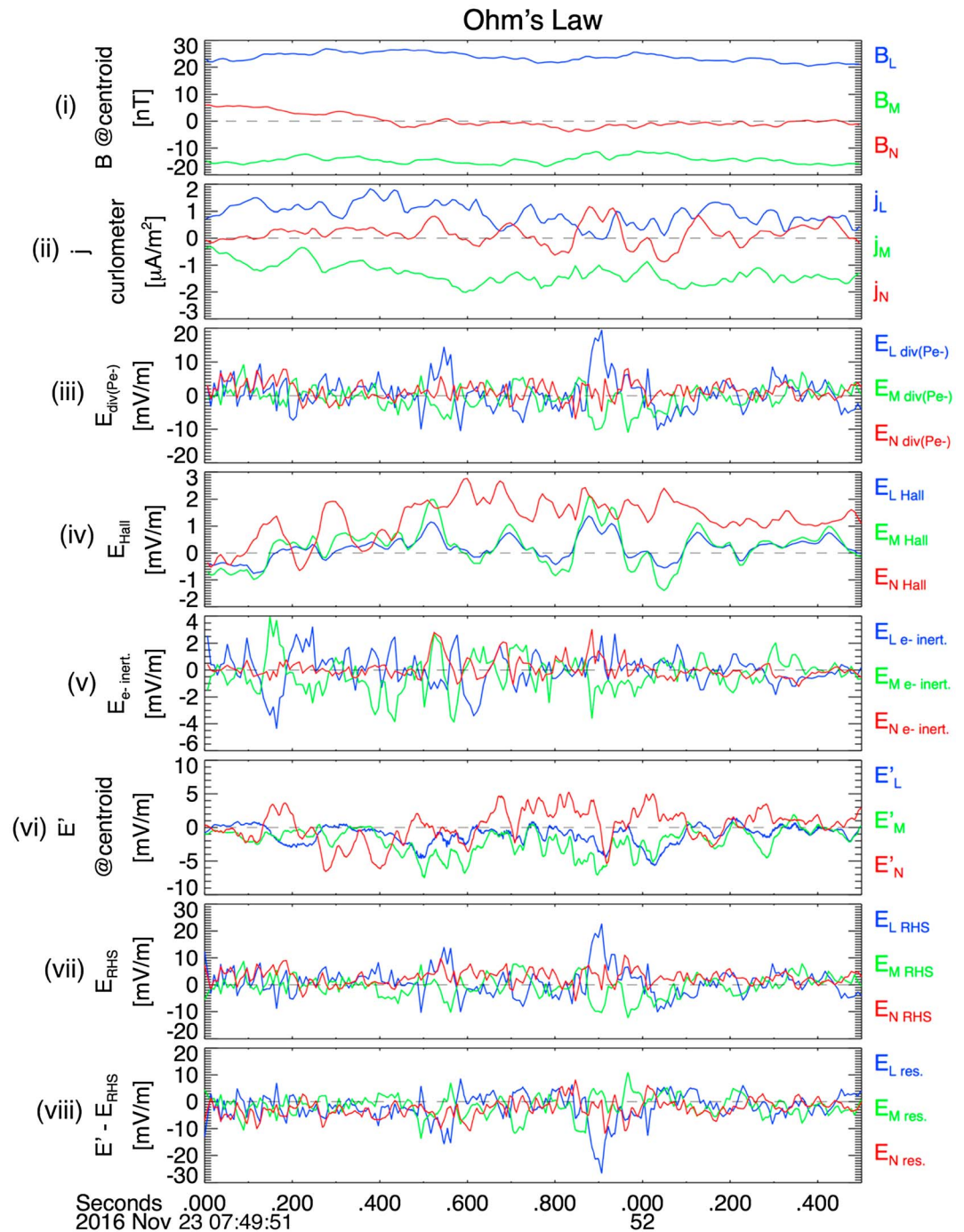
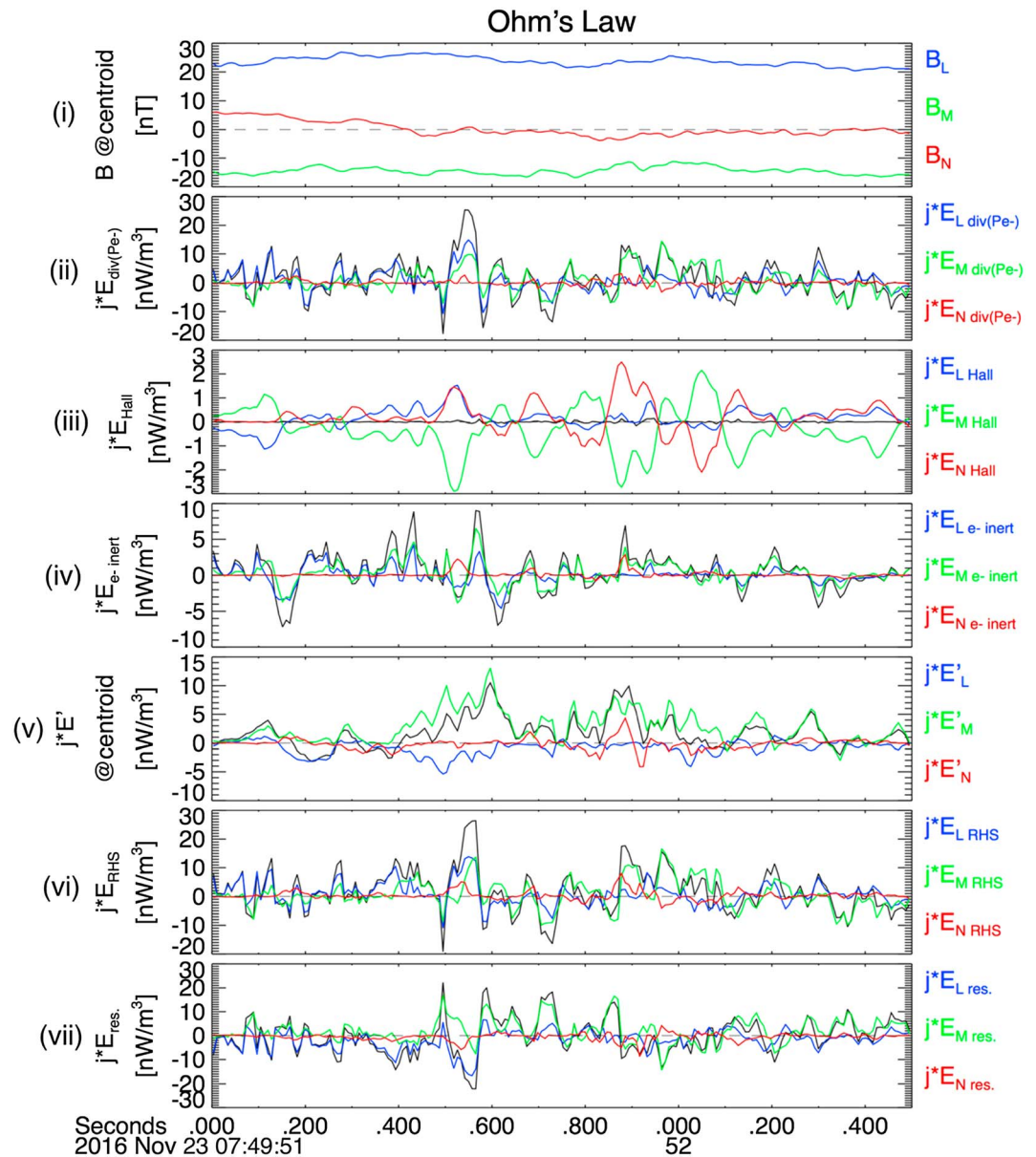


Figure 9. Ohm's law analysis during event 2. Panels are identical to Figure 8.

host to large amounts of turbulence, due to the large amplitudes of the nonideal Ohm's law terms and their generally chaotic behavior. Similar to the predictions of Price et al. (2016) (and Price et al., 2017), the turbulence was noticeably greater as MMS arrived at the reconnection symmetry plane from the southern cusp of the EDR. The degree to which this turbulence may invalidate the linear fit assumption used to derive the electron pressure tensor divergence and inertial terms is not yet quantified. Figure 10 shows a term-by-term breakdown of Ohmic energy conversion, and includes a very large, steady  $\mathbf{j} \cdot \mathbf{E}'$  measurement inferred at the barycenter. We interpret this as evidence that the heart of an EDR resided inside of the spacecraft tetrahedron for  $\sim 1$  s, host to fast reconnection ( $\mathbf{j} \cdot \mathbf{E}' > 4$  nW/m<sup>3</sup>). Positive  $\mathbf{j} \cdot \mathbf{E}'$  was





**Figure 10.** Ohm's law analysis of energy conversion during event 2. Panel (i) shows the  $B$  field again, for reference. Panel (ii) plots the energy conversion related to the divergence of the electron pressure tensor, panel (iii) is the Hall E-field energy conversion, and panel (iv) is electron inertial energy conversion. Panel (v) shows energy conversion in the electron rest frame. Panel (vi) is a summation of (ii) + (iii) + (iv), and panel (vii) is the energy conversion associated with the residual E-field.

confined to the  $M$  direction almost exclusively. MMS also observed a change in the residual energy conversion ( $\mathbf{j} \cdot \mathbf{E}_{res}$ ), which transitioned from predominantly negative values in  $L$  to positive values in  $M$  of similar amplitude as MMS passed through the  $M$ - $N$  plane of symmetry. The behavior strongly suggests a quasi-coherent spatial structure of the magnetosphere-side EDR related to Ohmic energy conversion and anomalous resistivity unlike any instance previously reported. Wave-particle interactions are a likely candidate driving some of this behavior, but the error introduced by the divergence and gradient computations and our exclusion of time dependence (along with other approximations) also bears consideration in a future study. We note that the large electrostatic pulses discussed in the analysis of event 2 (see the supporting information) did not coincide with obvious fluctuations or trends in any Ohm's law terms, nor did bursts of electrostatic wave activity of similar intensity seen in the MMS1 E-field spectrogram immediately surrounding the 1.5 s interval of event 2 studied in the supporting information.

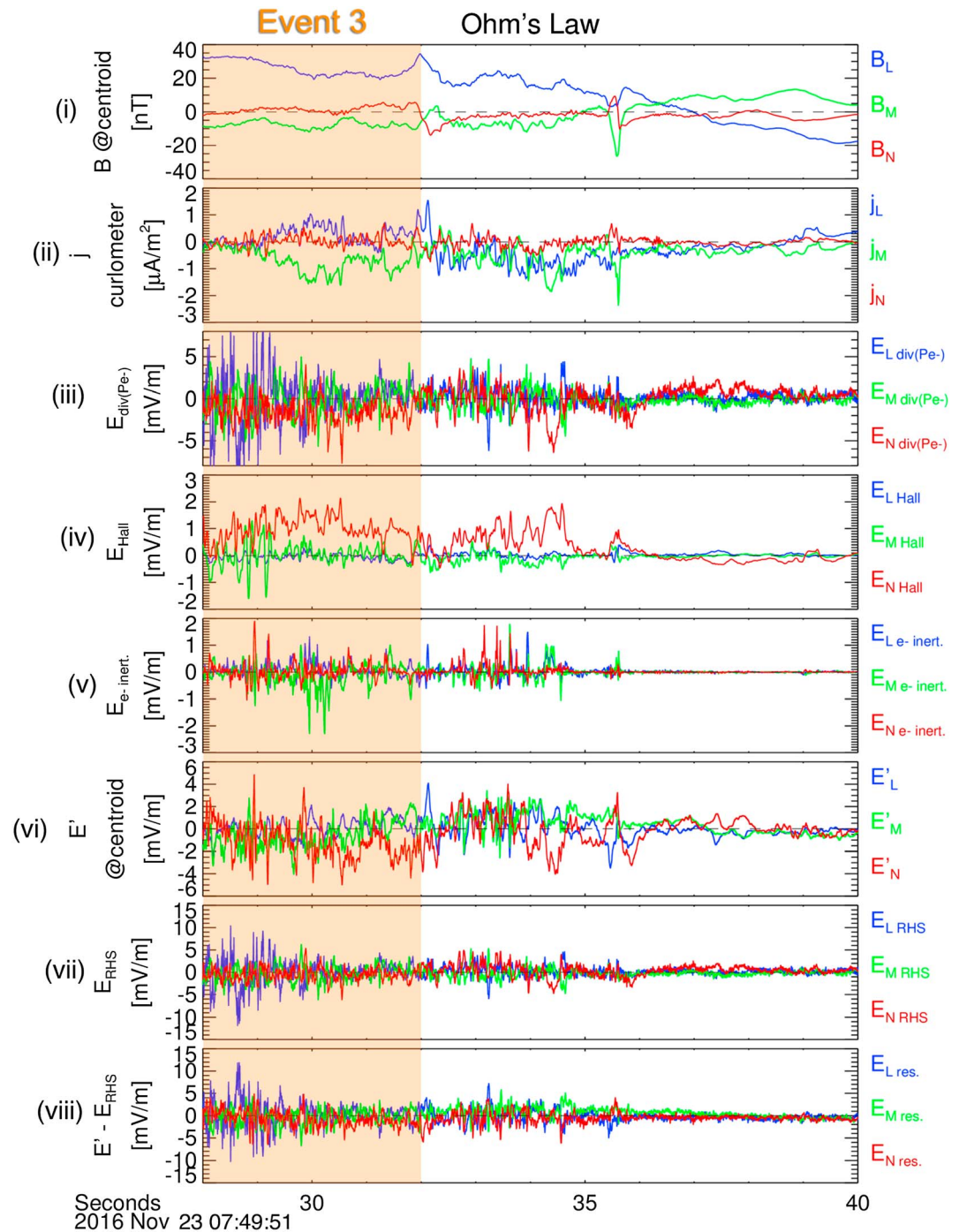


**Figure 11.** A 12-s duration Ohm's law analysis beginning at the start of event 3. Panels are identical to Figure 8.

The supporting videos show that other spacecraft also observed (nonsimultaneous) pulses of electrostatic waves near 100 mV/m during this interval, but neither did those pulses coincide with any clear fluctuations of Ohm's law terms. These findings all suggest that at least some meaningful electron-scale dynamics occur on distance scales smaller than the spacecraft separation (~6 km), especially near the center of the EDR. We note that the computations used to produce the Ohm's law plots have been qualified by almost perfectly reproducing previous works (Genestreti et al., 2018; Torbert et al., 2016), to within small fractions of mV/m or nW/m<sup>3</sup> discrepancy. Our comparatively large amplitude Ohm's law terms presented here should ensure a suitable signal-to-noise ratio for the large amplitude, sustained features we have focused on.

### 4.3.3. Event “3”

The spacecraft made a retreat earthward after event 2, and then reapproached the EDR from the magnetosphere again,  $\sim 40$  s later. More details are shown in the supporting information. An Ohm's law analysis of event 3 and the following 8 s (Figure 11) shows that  $\nabla \cdot \vec{P}_e$  dominated the nonideal terms once again, especially near the beginning of event 3, when MMS was furthest earthward, in the outer magnetosphere. Similar to event 1, the Hall term generally helped balance out the Ohm's law equation, canceling roughly one third to half of the  $E_N$  contribution from  $\nabla \cdot \vec{P}_e$ . During and after event 3, as MMS gradually approached the magnetopause, several periods of shared coherency occurred between sustained, negative  $E_N$  components of  $\nabla \cdot \vec{P}_e$  and  $\mathbf{E}'$ . The most prominent instance of agreement occurred near 07:50:34.3 UT, and lasted  $\sim 0.25$  s, while MMS resided inside of the magnetosphere electron current sheet (significant curlometer  $-j_M$ ). Excursions of  $E_N$  from  $\nabla \cdot \vec{P}_e$  toward zero and positive values seen in the magnetosphere typically coincided with abrupt cessations of  $-j_M$ , a self-consistency evident of a thin, oscillating current layer. A flux rope candidate at  $\sim 07:50:35.5$  UT caused disagreement between the  $N$  components of  $\mathbf{E}'$  and  $\nabla \cdot \vec{P}_e$ , although the two trended together again immediately afterwards.  $E_L$  and  $E_M$  for both  $\nabla \cdot \vec{P}_e$  and  $\mathbf{E}'$  are more difficult to characterize. As  $B_L$  reversed, so too did  $E_N$ , as MMS passed back into the magnetosheath. Electron pressure divergence enhancements ( $+E_N$ ) did not correspond as neatly with  $-j_M$  in the near-EDR sheath. The  $+E_N$  seen in the sheath was much greater during event 1 ( $\sim 6$  mV/m for event 1 versus  $\sim 2$  mV/m here), when a stronger current layer was present. Back inside the magnetosphere-side current sheet, near 07:50:30 UT in Figure 23(v), MMS recorded enhanced  $-E_M$  from the electron inertial term ( $\sim -2$  mV/m), several factors larger than a similar measurement reported by Torbert et al. (2016). A plot of the Ohmic energy conversion reveals a sustained electron inertial energy exchange simultaneously (see the supporting information) and suggests a direct energization of electrons by the reconnection  $E$  field. At the end of the 4 s event 3 interval, MMS saw the ion jet quickly reverse to positive values (Figure 7v), an onset of  $-j_L$  (Figure 11ii), and  $B_N$  reversing polarity (Figure 11i), all indications of another  $M$ - $N$  symmetry plane traversal. Large-amplitude fluctuations of  $\nabla \cdot \vec{P}_e$  ( $\sim 10$  mV/m) like those in event 2 are not found here, likely due to a quick sunward expansion of the reconnection system at the same instant (large  $+B_L, j_M \sim 0$ ). Additional Ohm's law plots in the supporting information reinforce some of the characteristics we have focused on and suggest that the intervals between our three events also contain relevant reconnection physics.

## 5. Conclusions

We presented a total of 32 EDR events or strong candidates, the majority of which are listed here for the first time. Nominal mission success for the dayside phase of MMS was contingent on 16 EDR encounters, a number we here show to have surpassed. Our collection of encounters illustrates a considerable variance of plasma conditions under which MMS has observed electron diffusion. Further characterizing this range of parameter space is difficult, and beyond the scope of this study. As predicted in simulations, PSD configurations exhibited by electron distributions in the EDR typically consist of a thermalized core population collocated with the energized crescent contribution responsible for producing a bulk flow perpendicular to  $\mathbf{B}$ . The three-dimensional electron data show that the crescents are more similar to a partial toroid than to a hemispherical shell. The meta-study showed positive correlations between the observed agyrotropy and the Ohmic energy exchange and current densities. The IMF  $Y$ -component polarity influenced the locations of the EDR events, and global magnetosphere modeling using the 23 November 2016 solar wind conditions predicted an enhancement of the  $B$  field  $Y$  component in both the magnetosphere and magnetosheath as field lines from each approached the reconnection site. MMS observations of a significant guide field ( $\sim 1/2$ ) at the 23 November 2016 EDR sites are at least somewhat consistent with the model's predictions.

Using the three 23 November 2016 events, we have demonstrated new relationships between several measures used to gauge EDR activity, including  $\mathbf{j} \cdot \mathbf{E}'$ , agyrotropy, crescent-shaped velocity distributions, electron heating, large  $|\mathbf{j}|$ , and low-frequency ( $\sim 10$  Hz) waves across multiple measurements. These events spanned  $\sim 1$  min and show that reconnection can occur locally over minute-long time scales. Notable gradients in the magnetic field ( $\sim 2$  nT/km) and temperature ( $\sim 5$  eV/km) were present. The gradients were proved (to first order) a function of relative spacecraft positions projected onto the  $N$  axis of a boundary-normal coordinate system. During event 2, simultaneous measurements were made on open and closed field lines, above and below the  $M$ - $N$  symmetry plane, and are unprecedented for MMS and thus for any measurement of

reconnection in space. Waveforms similar to electrostatic whistlers known to contain sheets of trapped electrons were present at the symmetry plane traversal during event 2. An Ohm's law analysis showed a general dominance of  $\nabla \cdot \vec{P}_e$  over all other terms, especially during event 2, but the exact behavior varied significantly between our three events. Nonideal Ohmic energy conversion was also usually dominated by  $\nabla \cdot \vec{P}_e$ . Generally, if MMS was located in the electron current sheet, an agreement arose between  $\mathbf{E}'$  and  $\nabla \cdot \vec{P}_e$ , with both showing  $-E_N$  on the magnetosphere side, and  $+E_N$  on the magnetosheath side. Ohmic energy exchange was also most coherent inside of the current sheet, and typically confined to the  $L$  and  $M$  directions. Chaotic behavior of Ohm's law terms, likely indicative of turbulence, was seen predominantly on the magnetosphere side of the EDR, near the  $M$ - $N$  symmetry plane.

### Acknowledgments

We thank the MMS instrument team leaders for working to achieve this high-resolution, multispacecraft data: R. Nakamura for the Active Spacecraft Potential Control (ASPOC), B. H. Mauk for the Energetic Particle Instrument (EPI) data, and R. J. Strangeway for the magnetic field data. Contributions from the entire MMS Science Working Team (SWT) aided this study. The SPEDAS (Space Physics Environment Data Analysis System) software package, used for data querying, parsing, and visualization, greatly aided in expediting our research. The authors are also grateful to the MMS Science Data Center (SDC) of the Laboratory for Atmospheric and Space Physics (LASP) for hosting the large database of MMS observations, found here: <https://lasp.colorado.edu/mms/sdc/public/links/>. We thank CDAWeb data provider J. H. King, N. Papatashvili at AdnetSystems, and NASA GSFC for the OMNI data. This study was supported by NASA under grants NNX14AN55G and NNG04EB99C.

### References

- Argall, M. R., Paulson, K., Alm, L., Rager, A., Dorelli, J., Shuster, J., et al. (2018). Electron dynamics within the electron diffusion region of asymmetric reconnection. *Journal of Geophysical Research: Space Physics*, *123*, 146–162. <https://doi.org/10.1002/2017JA024524>
- Burch, J. L., Moore, T. E., Torbert, R. B., & Giles, B. L. (2016). Magnetospheric multiscale overview and science objectives. *Space Science Reviews*, *199*(1–4), 5–21. <https://doi.org/10.1007/s11214-015-0164-9>
- Burch, J. L., & Phan, T. D. (2016). Magnetic reconnection at the dayside magnetopause: Advances with MMS. *Geophysical Research Letters*, *43*, 8327–8338. <https://doi.org/10.1002/2016GL069787>
- Burch, J. L., Torbert, R. B., Phan, T. D., Chen, L. J., Moore, T. E., Ergun, R. E., et al. (2016). Electron-scale measurements of magnetic reconnection in space. *Science*, *352*(6290), aaf2939. <https://doi.org/10.1126/science.aaf2939>
- Cattell, C., Dombek, J., Wygant, J., Drake, J. F., Swisdak, M., Goldstein, M. L., et al. (2005). Cluster observations of electron holes in association with magnetotail reconnection and comparison to simulations. *Journal of Geophysical Research*, *110*, A01211. <https://doi.org/10.1029/2004JA010519>
- Chen, L.-J., Hesse, M., Wang, S., Gershman, D., Ergun, R., Pollock, C., et al. (2016). Electron energization and mixing observed by MMS in the vicinity of an electron diffusion region during magnetopause reconnection. *Geophysical Research Letters*, *43*, 6036–6043. <https://doi.org/10.1002/2016GL069215>
- Chen, L.-J., Hesse, M., Wang, S., Gershman, D., Ergun, R. E., Burch, J., et al. (2017). Electron diffusion region during magnetopause reconnection with an intermediate guide field: Magnetospheric multiscale observations. *Journal of Geophysical Research: Space Physics*, *122*, 5235–5246. <https://doi.org/10.1002/2017JA024004>
- Drake, J. F., Kleva, R. G., & Mandt, M. E. (1994). Structure of thin current layers: Implications for magnetic reconnection. *Physical Review Letters*, *73*(9), 1251–1254. <https://doi.org/10.1103/PhysRevLett.73.1251>
- Drake, J. F., Swisdak, M., Cattell, C., Shay, M. A., Rogers, B. N., & Zeiler, A. (2003). Formation of electron holes and particle energization during magnetic reconnection. *Science*, *299*(5608), 873–877. <https://doi.org/10.1126/science.1080333>
- Ergun, R. E., Chen, L. J., Wilder, F. D., Ahmadi, N., Eriksson, S., Usanova, M. E., et al. (2017). Drift waves, intense parallel electric fields, and turbulence associated with asymmetric magnetic reconnection at the magnetopause. *Geophysical Research Letters*, *44*, 2978–2986. <https://doi.org/10.1002/2016GL072493>
- Ergun, R. E., Tucker, S., Westfall, J., Goodrich, K. A., Malaspina, D. M., Summers, D., et al. (2016). The axial double probe and fields signal processing for the MMS mission. *Space Science Reviews*, *199*(1–4), 167–188. <https://doi.org/10.1007/s11214-014-0115-x>
- Eriksson, S., Lavraud, B., Wilder, F. D., Stawarz, J. E., Giles, B. L., Burch, J. L., et al. (2016). Magnetospheric Multiscale observations of magnetic reconnection associated with Kelvin-Helmholtz waves. *Geophysical Research Letters*, *43*, 5606–5615. <https://doi.org/10.1002/2016GL068783>
- Fuselier, S. A., Vines, S. K., Burch, J. L., Petrinesc, S. M., Trattner, K. J., Cassak, P. A., et al. (2017). Large-scale characteristics of reconnection diffusion regions and associated magnetopause crossings observed by MMS. *Journal of Geophysical Research: Space Physics*, *122*, 5466–5486. <https://doi.org/10.1002/2017JA024024>
- Genestreti, K. J., Varsani, A., Burch, J. L., Cassak, P. A., Torbert, R. B., Nakamura, R., et al. (2018). MMS observation of asymmetric reconnection supported by 3-D electron pressure divergence. *Journal of Geophysical Research: Space Physics*, *123*, 1806–1821. <https://doi.org/10.1002/2017JA025019>
- Graham, D. B., Khotyaintsev, Y. V., Vaivads, A., Norgren, C., André, M., Webster, J. M., et al. (2017). Instability of agyrotropic electron beams near the electron diffusion region. *Physical Review Letters*, *119*(2), 025101. <https://doi.org/10.1103/PhysRevLett.119.025101>
- Gurnett, D., & Bhattacharjee, A. (2005). *Introduction to Plasma Physics*, (6.1.17 ed. p. 179). Cambridge, UK: Cambridge University press.
- Hesse, M., Aunai, N., Sibeck, D., & Birn, J. (2014). On the electron diffusion region in planar, asymmetric systems. *Geophysical Research Letters*, *41*, 8673–8680. <https://doi.org/10.1002/2014GL061586>
- Hesse, M., Liu, Y. H., Chen, L. J., Bessho, N., Kuznetsova, M., Birn, J., & Burch, J. L. (2016). On the electron diffusion region in asymmetric reconnection with a guide magnetic field. *Geophysical Research Letters*, *43*, 2359–2364. <https://doi.org/10.1002/2016GL068373>
- Hwang, K.-J., Goldstein, M. L., Wendel, D. E., Fazakerley, A. N., & Gurgiolo, C. (2013). Cluster observations near reconnection X lines in Earth's magnetotail current sheet. *Journal of Geophysical Research: Space Physics*, *118*, 4199–4209. <https://doi.org/10.1002/jgra.50403>
- Kellogg, P. J., Cattell, C. A., Goetz, K., Monson, S. J., & Wilson, L. B. III (2010). Electron trapping and charge transport by large amplitude whistlers. *Geophysical Research Letters*, *37*, L20106. <https://doi.org/10.1029/2010GL044845>
- Khotyaintsev, Y. V., Graham, D. B., Norgren, C., Eriksson, E., Li, W., Johlander, A., et al. (2016). Electron jet of asymmetric reconnection. *Geophysical Research Letters*, *43*, 5571–5580. <https://doi.org/10.1002/2016GL069064>
- Khotyaintsev, Y. V., Vaivads, A., André, M., Fujimoto, M., Retinò, A., & Owen, C. J. (2010). Observations of slow electron holes at a magnetic reconnection site. *Physical Review Letters*, *105*(16), 165002. <https://doi.org/10.1103/PhysRevLett.105.165002>
- Khrabrov, A. V., & Sonnerup, B. U. Ö. (1998). Orientation and motion of current layers: Minimization of the Faraday residue. *Geophysical Research Letters*, *25*(13), 2373–2376. <https://doi.org/10.1029/98GL51784>
- Le Contel, O., et al. (2014). The search-coil magnetometer for MMS. *Space Science Reviews*, *199*(1–4), 257–282. <https://doi.org/10.1007/s11214-014-0096-9>
- Lindqvist, P.-A., Olsson, G., Torbert, R. B., King, B., Granoff, M., Rau, D., et al. (2016). The spin-plane double probe electric field instrument for MMS. *Space Science Reviews*, *199*(1–4), 137–165. <https://doi.org/10.1007/s11214-014-0116-9>

- Norgren, C., Graham, D. B., Khotyaintsev, Y. V., André, M., Vaivads, A., Chen, L. J., et al. (2016). Finite gyroradius effects in the electron outflow of asymmetric magnetic reconnection. *Geophysical Research Letters*, *43*, 6724–6733. <https://doi.org/10.1002/2016GL069205>
- Petrinec, S. M., Burch, J. L., Fuselier, S. A., Gomez, R. G., Lewis, W., Trattner, K. J., et al. (2016). Comparison of Magnetospheric Multiscale ion jet signatures with predicted reconnection site locations at the magnetopause. *Geophysical Research Letters*, *43*, 5997–6004. <https://doi.org/10.1002/2016GL069626>
- Phan, T. D., Eastwood, J. P., Cassak, P. A., Øieroset, M., Gosling, J. T., Gershman, D. J., et al. (2016). MMS observations of electron-scale filamentary currents in the reconnection exhaust and near the X line. *Geophysical Research Letters*, *43*, 6060–6069. <https://doi.org/10.1002/2016GL069212>
- Pollock, C. J., Moore, T., Jacques, A., Burch, J., Gliese, U., Saito, Y., et al. (2016). Fast plasma investigation for Magnetospheric Multiscale. *Space Science Reviews*, *199*(1–4), 331–406. <https://doi.org/10.1007/s11214-016-0245-4>
- Price, L. M., Swisdak, M., Drake, J. F., Burch, J. L., Cassak, P. A., Ergun, R. E., et al. (2017). Turbulence in three-dimensional simulations of magnetopause reconnection. *Journal of Geophysical Research: Space Physics*, *122*, 11,086–11,099. <https://doi.org/10.1002/2017JA024227>
- Price, L. M., Swisdak, M., Drake, J. F., Cassak, P. A., Dahlin, J. T., & Ergun, R. E. (2016). The effects of turbulence on three-dimensional magnetic reconnection at the magnetopause. *Geophysical Research Letters*, *43*, 6020–6027. <https://doi.org/10.1002/2016GL069578>
- Rager, A. C., Dorelli, J. C., Gershman, D. J., Uritsky, V., Avakov, L. A., Torbert, R. B., et al. (2018). Electron crescent distributions as a manifestation of diamagnetic drift in an electron-scale current sheet: Magnetospheric Multiscale observations using new 7.5 ms Fast Plasma Investigation moments. *Geophysical Research Letters*, *45*, 578–584. <https://doi.org/10.1002/2017GL076260>
- Russell, C. T., Anderson, B. J., Baumjohann, W., Bromund, K. R., Dearborn, D., Fischer, D., et al. (2016). The magnetospheric multiscale magnetometers. *Space Science Reviews*, *199*(1–4), 189–256. <https://doi.org/10.1007/s11214-014-0057-3>
- Shay, M. A., Phan, T. D., Haggerty, C. C., Fujimoto, M., Drake, J. F., Malakit, K., et al. (2016). Kinetic signatures of the region surrounding the X line in asymmetric (magnetopause) reconnection. *Geophysical Research Letters*, *43*, 4145–4154. <https://doi.org/10.1002/2016GL069034>
- Swisdak, M. (2016). Quantifying gyrotopology in magnetic reconnection. *Geophysical Research Letters*, *43*, 43–49. <https://doi.org/10.1002/2015GL066980>
- Tang, X., Cattell, C., Dombeck, J., Dai, L., Wilson, L. B. III, Breneman, A., & Hupach, A. (2013). THEMIS observations of the magnetopause electron diffusion region: Large amplitude waves and heated electrons. *Geophysical Research Letters*, *40*, 2884–2890. <https://doi.org/10.1002/grl.50565>
- Torbert, R. B., Burch, J. L., Giles, B. L., Gershman, D., Pollock, C. J., Dorelli, J., et al. (2016). Estimates of terms in Ohm's law during an encounter with an electron diffusion region. *Geophysical Research Letters*, *43*, 5918–5925. <https://doi.org/10.1002/2016GL069553>
- Torbert, R. B., Russell, C. T., Magnes, W., Ergun, R. E., Lindqvist, P. A., LeContel, O., et al. (2016). The FIELDS instrument suite on MMS: Scientific objectives, measurements, and data products. *Space Science Reviews*, *199*(1–4), 105–135. <https://doi.org/10.1007/s11214-014-0109-8>
- Tóth, G., Sokolov, I. V., Gombosi, T. I., Chesney, D. R., Clauer, C. R., de Zeeuw, D. L., et al. (2005). Space weather modeling framework: A new tool for the space science community. *Journal of Geophysical Research*, *110*, A12226. <https://doi.org/10.1029/2005JA011126>
- Trattner, K. J., Burch, J. L., Ergun, R., Eriksson, S., Fuselier, S. A., Giles, B. L., et al. (2017). The MMS dayside magnetic reconnection locations during phase 1 and their relation to the predictions of the maximum magnetic shear model. *Journal of Geophysical Research*, *122*, 11,991–12,005. <https://doi.org/10.1002/2017JA024488>